

AD-A280 506 TION PAGE

Form Approved
OMB No. 0704-0188

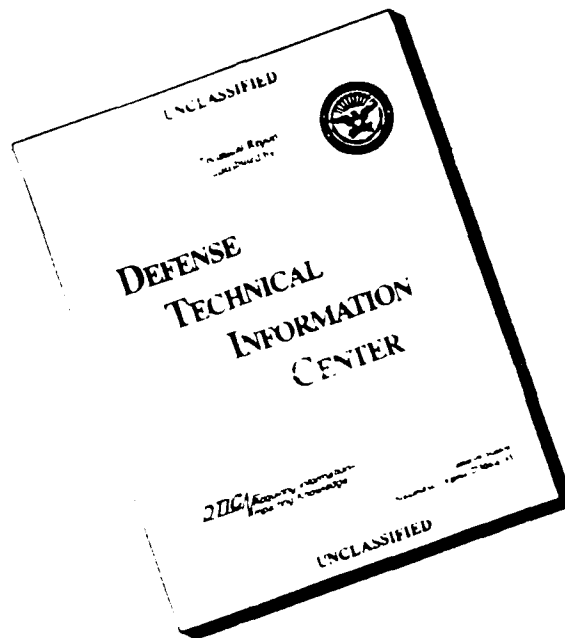
①

Pub
gov
collection of information
Data Highway, Suite 1204, Arlington, VA 22204-4302

Please allow for response, including the time for reviewing instructions, searching existing data sources, gathering the collection of information. Send comments regarding this burden estimate or any other aspect of this collection of information, including suggestions for reducing the burden, to Washington Headquarters Services, Directorate for Information Operations and Reports, 1215 Jefferson Davis Highway, Suite 1204, Arlington, VA 22204-4302, and to the Office of Management and Budget, Paperwork Reduction Project (0704-0188), Washington, DC 20503.

1. AGENCY USE ONLY (Leave blank)		2. REPORT DATE 27 May 94	3. REPORT TYPE AND DATES COVERED Final 1 Oct 91 - 30 Sep 93
4. TITLE AND SUBTITLE Fundamental Study of Hypersonic Unstart		5. FUNDING NUMBERS F49620-92-J-0006 2307/AS	
6. AUTHOR(S) Mark Lewis		DTIC ELECTE JUN 21 1994	
7. PERFORMING ORGANIZATION NAME(S) AND ADDRESS(ES) U of Maryland College Park MD 20742		8. PERFORMING ORGANIZATION REPORT NUMBER AEOSR-TR-94 0362	
9. SPONSORING/MONITORING AGENCY NAME(S) AND ADDRESS(ES) AIR FORCE OFFICE OF SCIENTIFIC RESEARCH DIRECTORATE OF AEROSPACE SCIENCES BOLLING AFB, DC 20332-6448		10. SPONSORING/MONITORING AGENCY REPORT NUMBER F49620-92-J-0006	
11. SUPPLEMENTARY NOTES			
12a. DISTRIBUTION/AVAILABILITY STATEMENT APPROVED FOR PUBLIC RELEASE DISTRIBUTION IS UNLIMITED		12b. DISTRIBUTION CODE DTIC QUALITY INSPECTED 2	
13. ABSTRACT (Maximum 200 words) <p>Activities for the first year were primarily focused on laying the groundwork for accomplishing the ultimate goals of this investigation. Required hardware and software was obtained and implemented. Grid generators were tested and one was selected, as was the primary computational tool.</p> <p>Activities in the second year were directed towards beginning the three-dimensional Euler, then Navier-Stokes calculations, to establish a steady-state time accurate baseline, which could then be perturbed to study the influence of downstream disturbances. Both Euler and laminar Navier-Stokes solutions were calculated.</p>			
14. SUBJECT TERMS Hypersonic, Euler, Unstart		15. NUMBER OF PAGES 75	
16. PRICE CODE		17. SECURITY CLASSIFICATION OF REPORT UNCLASSIFIED	
18. SECURITY CLASSIFICATION OF THIS PAGE UNCLASSIFIED		19. SECURITY CLASSIFICATION OF ABSTRACT UNCLASSIFIED	
20. LIMITATION OF ABSTRACT			

DISCLAIMER NOTICE



THIS REPORT IS INCOMPLETE BUT IS THE BEST AVAILABLE COPY FURNISHED TO THE CENTER. THERE ARE MULTIPLE MISSING PAGES. ALL ATTEMPTS TO DATE TO OBTAIN THE MISSING PAGES HAVE BEEN UNSUCCESSFUL.

Final Report:

A Fundamental Study of Hypersonic Unstarts

Mark J. Lewis

AFOSR-JR- 94 0362

Overview

Approved for public release;
distribution unlimited.

The goals of this project were to attempt to simulate a fully viscous, three-dimensional time accurate hypersonic inlet/engine combined geometry, for the specific purposes of studying the fundamental physics associated with the phenomena of engine unstarts. Particular interest was initially placed on the interaction between the inlet shock structure and the viscous boundary layer, especially in examining the growth of separation regions and the communication of downstream perturbations to the upstream inlet shock structure.

Activities for the first year were primarily focused on laying the groundwork for accomplishing the ultimate goals of this investigation. Required hardware and software was obtained and implemented. Grid generators were tested and one was selected, as was the primary computational tool. On the technical side, a substantial literature search was conducted. Several papers with hypersonic inlet and engine flowfields were located, and have been used for code validation. A baseline geometry was selected for both 2-D and 3-D calculations, based on the availability of data for comparison.

Gridding was completed for these geometries. A detailed study of the time accuracy of the code, vital to this project, was undertaken. Two validation cases were considered: a quasi-one-dimensional shock tube, for validating internal flows (i.e. combustor flowfields) and a 24° compression corner, for validating external flows (i.e. forebody inlets). Extensive comparisons between the GASP results, analytical solutions, and other time-accurate codes were made.

94 6 20 04 1

65P8
94-18974



Finally, time accurate studies on the flow inside the combustor channel were begun in the first period. Preliminary work examined the separation region associated with an unexpected (off-design) shock-boundary layer impingement inside the engine channel, and the resulting upstream propagation of that disturbance.

Activities in the second year were directed towards beginning the three-dimensional Euler, then Navier-Stokes calculations, to establish a steady-state time accurate baseline, which could then be perturbed to study the influence of downstream disturbances. Both Euler and laminar Navier-Stokes solutions were calculated, though problems with an ever-expanding separation zone in the laminar-flow regime prevented the establishment of steady-state conditions.

Hardware and Software Support

In support of the technical accomplishments of this work, the following tasks were completed:

- Purchasing (with university funds) and installing a Silicon Graphics Indigo Elan workstation which is dedicated for this project. Substantial time was invested in setting up that system and obtaining and installing appropriate software.
- Obtaining several grid generation packages, including EAGLE and EAGLEVIEW from Mississippi State University, and becoming familiar with the operation of these codes.
- Installing and becoming familiar with Walter's GASP code as the primary computational tool, and modifying that code to facilitate time-accurate solutions.
- Installing and becoming familiar with a graphics package (the FAST code from NASA Ames) for data presentation.

Availability Codes	
Dist	Avail and / or Special
A-1	

A major portion of this research project, run in parallel with the validation and numerical experimentation with the computational tool, was the selection, implementation, and familiarization with a three-dimensional grid generator. To this end, several grid generation programs were considered, including GRIDGEN, EAGLE, and EAGLEVIEW (an interactive EAGLE derivative.)

The batch version of the EAGLE code was first used to generate a typical 3-D computational grid in the Langley 3-D module geometry. Figure 21 is a representation of one such result. The wall geometry itself, extracted from the grid, is shown in Figure 22. Note the sidewall compression, and the fact that a foreplate is used to produce an inlet boundary layer. For the work of interest here, final results will likely be performed with the inlet forebody canted at a more representative angle, or with a preset boundary layer profile. One of the ultimate interests in this study is the inclusion of boundary layer effects, and the coupling of these to the unsteady shock behavior, so inclusion of a realistic forebody flowfield is of importance. Euler flow calculations were performed in a two dimensional cross-section of the above geometry for a baseline indication of the associated shock structure. Figure 23 shows density contours and variations along the centerline through the engine.

The time response of the 2-D RPI combustor flowfield was calculated with GASP, using a 251×101 grid covering the inlet, combustor, and nozzle region of that engine shape, shown in Figure 24. That inlet is not designed with a shock-on-lip configuration, so a strong shock reflects into the engine channel and strikes the combustor wall boundary layer. This interaction generates a separated region which propagates upstream from the intersection point.

Figure 25 shows the density and Mach number contours in this engine at freestream Mach number 6. The relatively strong reflected shock is visible, as is the thick boundary layer. For these calculations the boundary layer was kept laminar, though in reality it will likely be turbulent past the ramp; a turbulent boundary layer will exhibit a much smaller separation region with a shock interaction, so the separated region is exaggerated.

Code Selection and Validation

For purposes of studying the fundamental physics of this problem, it was necessary to locate a computational tool which was time-accurate, three-dimensional, and had features for including chemical models. To this end, several existing codes were examined. The TVD scheme of Yee, et. al. has been used successfully by the principal investigator for both 2-D and axisymmetric calculations but extension to three-dimensions would have represented a monumental effort. Similarly, CFL3D has also been used at Maryland, but does not include chemistry, and so was not adopted.

The General Aerodynamic Simulation Program (GASP) of Walters, et. al. was chosen because it had all of the required features, and was advertised (though not validated) as time-accurate. The first task in using GASP, after becoming familiar with its operation, was, therefore, to validate the time-accuracy, after modifying the code to facilitate restart and periodic output.

Two cases were considered:

- Internal hypersonic flow in a shock tube (one-dimensional flow, but calculated in two dimensions.)
- External hypersonic flow on Holden's 24-degree compression corner.

The shock tube calculation is shown in Figure 1, which presents density variation along the tube as a function of distance along the centerline, for a given pressure ratio, using Roe's flux difference splitting. This is compared to the exact Riemann solution at .5 ms. Note the excellent agreement between the results. Temperature and velocity are shown in Figures 2 and 3, and they also compare quite well with the exact solutions. Corresponding thermodynamic contours are shown in Figure 4

Subsequent studies were done examining different time-integration schemes. Figure 5 shows a comparison of two-factor approximate factorization and a Jameson m -stage Runge-Kutta method. The implicit

Density variation along centerline of a Shock Tube
Comparison between exact and CFD solution

$P_4 / P_1 = 3.061$
 $W = 432.0 \text{ m/s}$
 $U_p = 136.1 \text{ m/s}$

Elapsed time = 0.5 ms

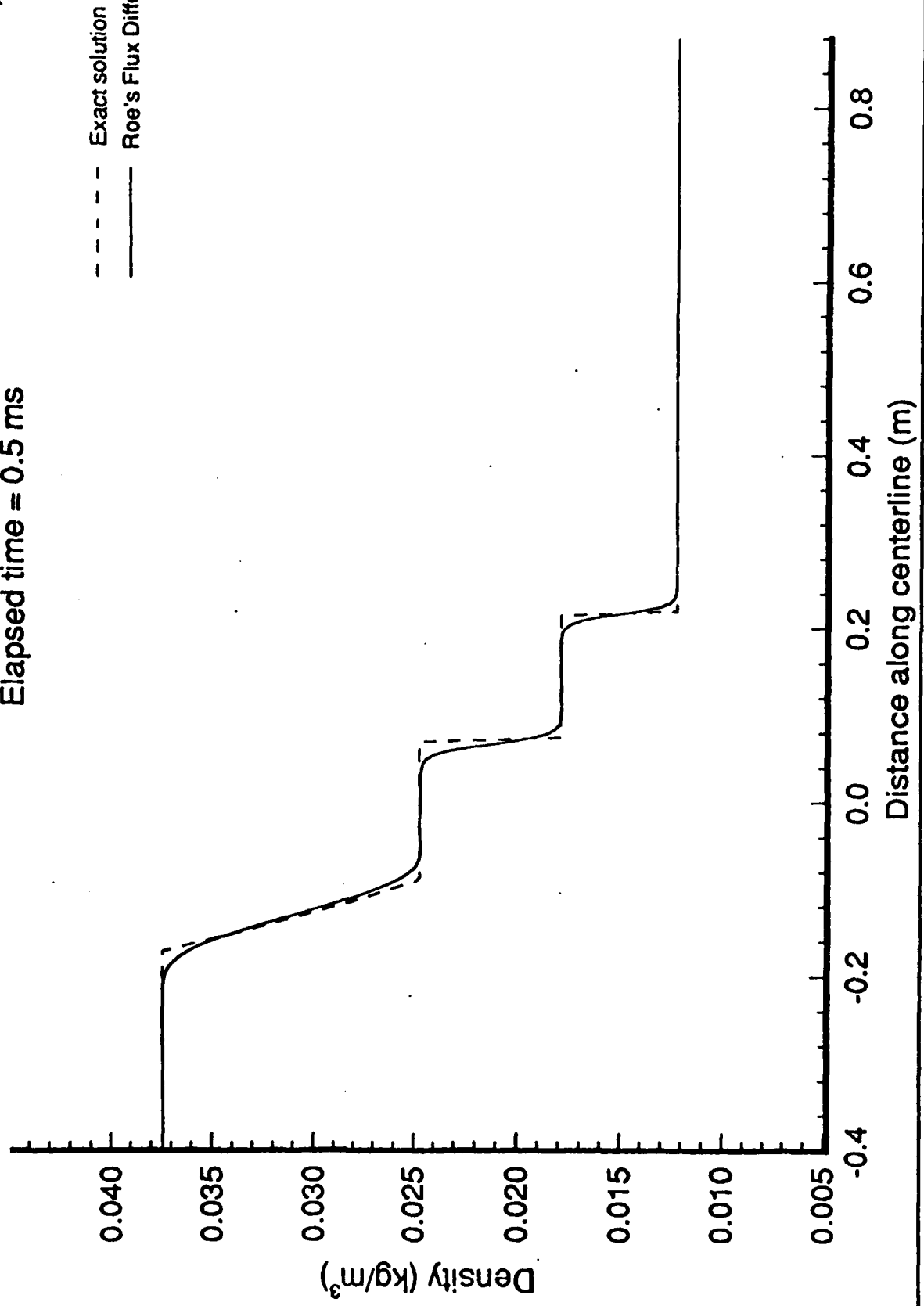


Figure 1

Temperature variation along the centerline of the Shock Tube

Elapsed time = 5.0E-4 s

invfixi = invfixj = 3

rkapi = rkapj = 1/3

limi = limj = 3

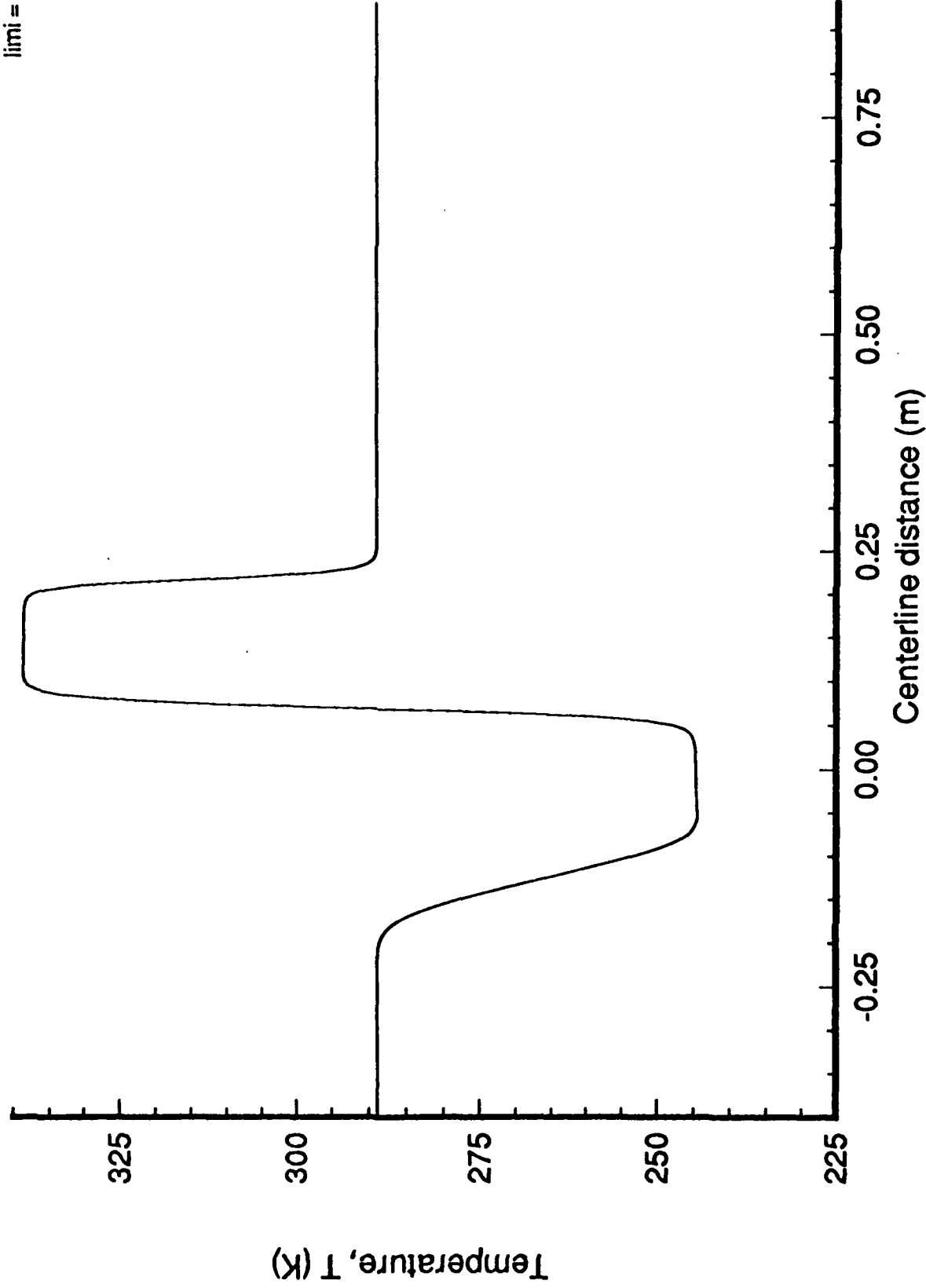


Figure 2

Velocity(u) variation along the centerline of the Shock Tube

Elapsed time = 5.0E-4 s

invfixi = invfixj = 3

rkapi = rkapij = 1/3

limi = limj = 3

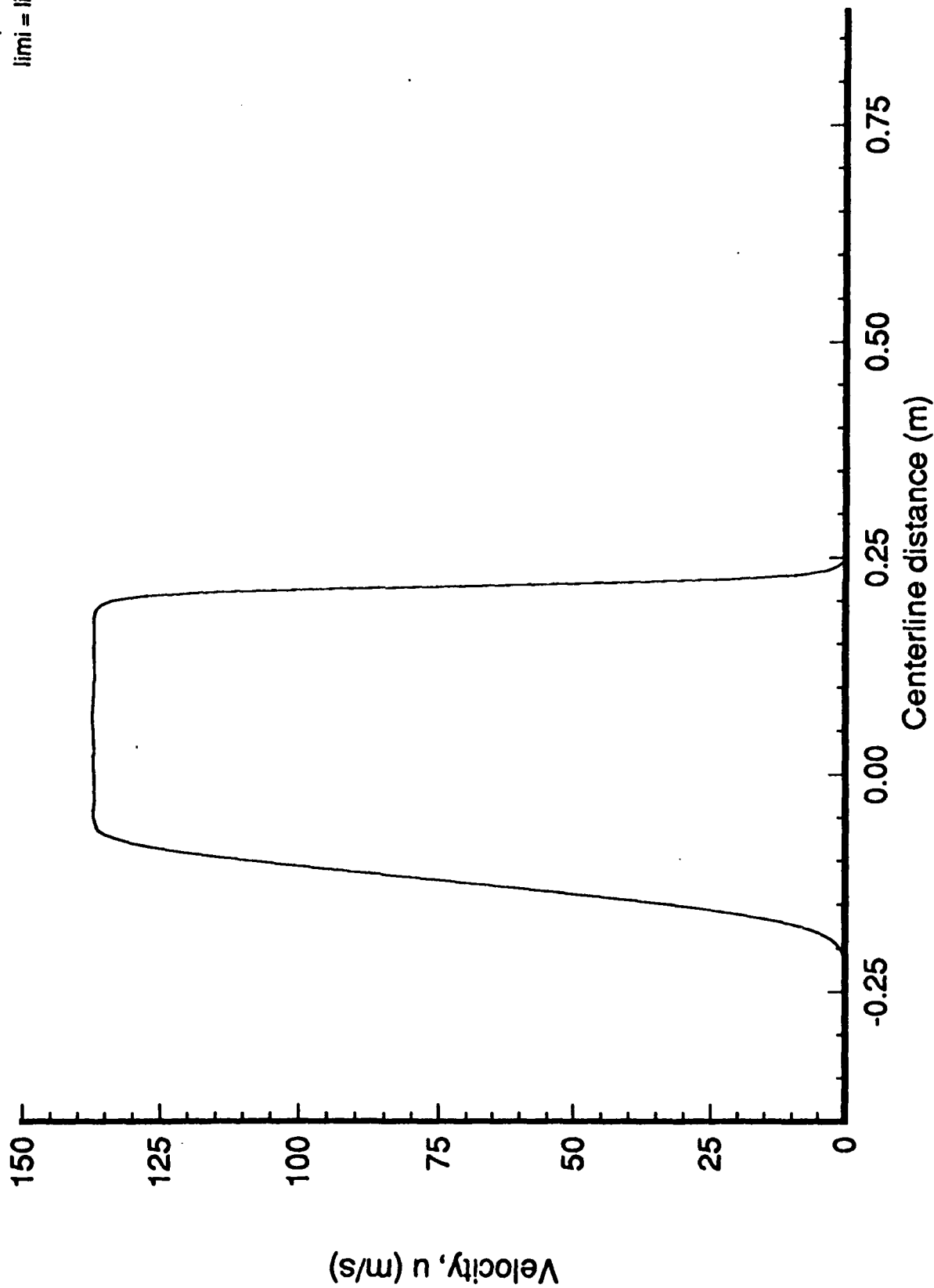
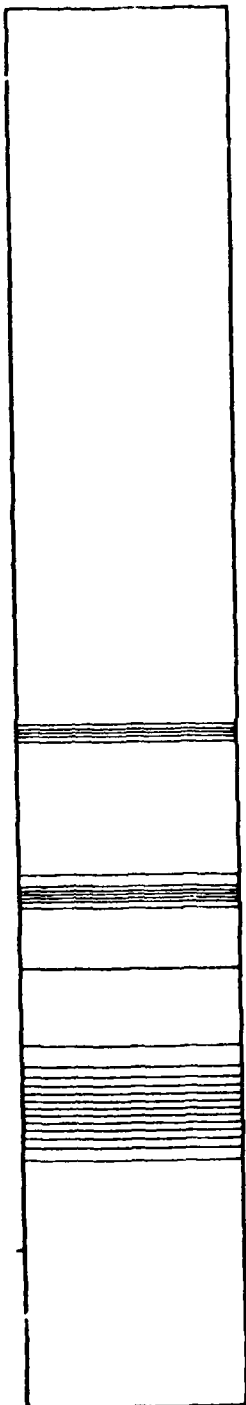
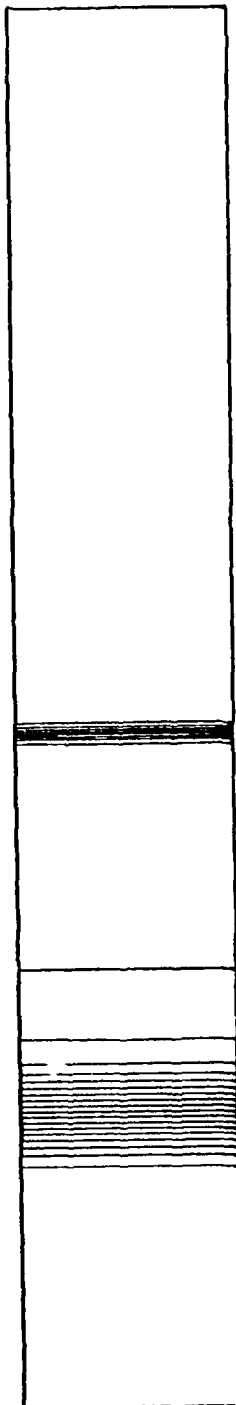


Figure 3

Density contours in Shock Tube



Pressure contours in Shock Tube



Temperature contours in Shock Tube

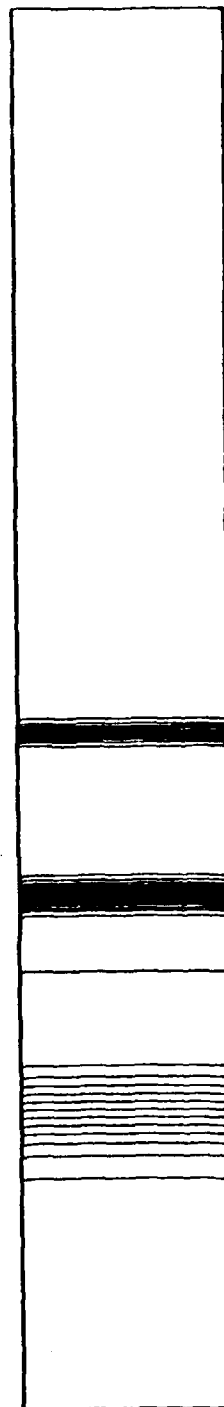


Figure 4

Density variation along the centerline of the Shock Tube

Comparison of time integration schemes

- 2-Factor Approximate Factorization
- m-stage Runge-Kutta

Elapsed time = 5.0E-4 s
invfixi = invfixj = 3
rkapi = rkapij = 1/3
limi = limj = 3

2-F AF

□

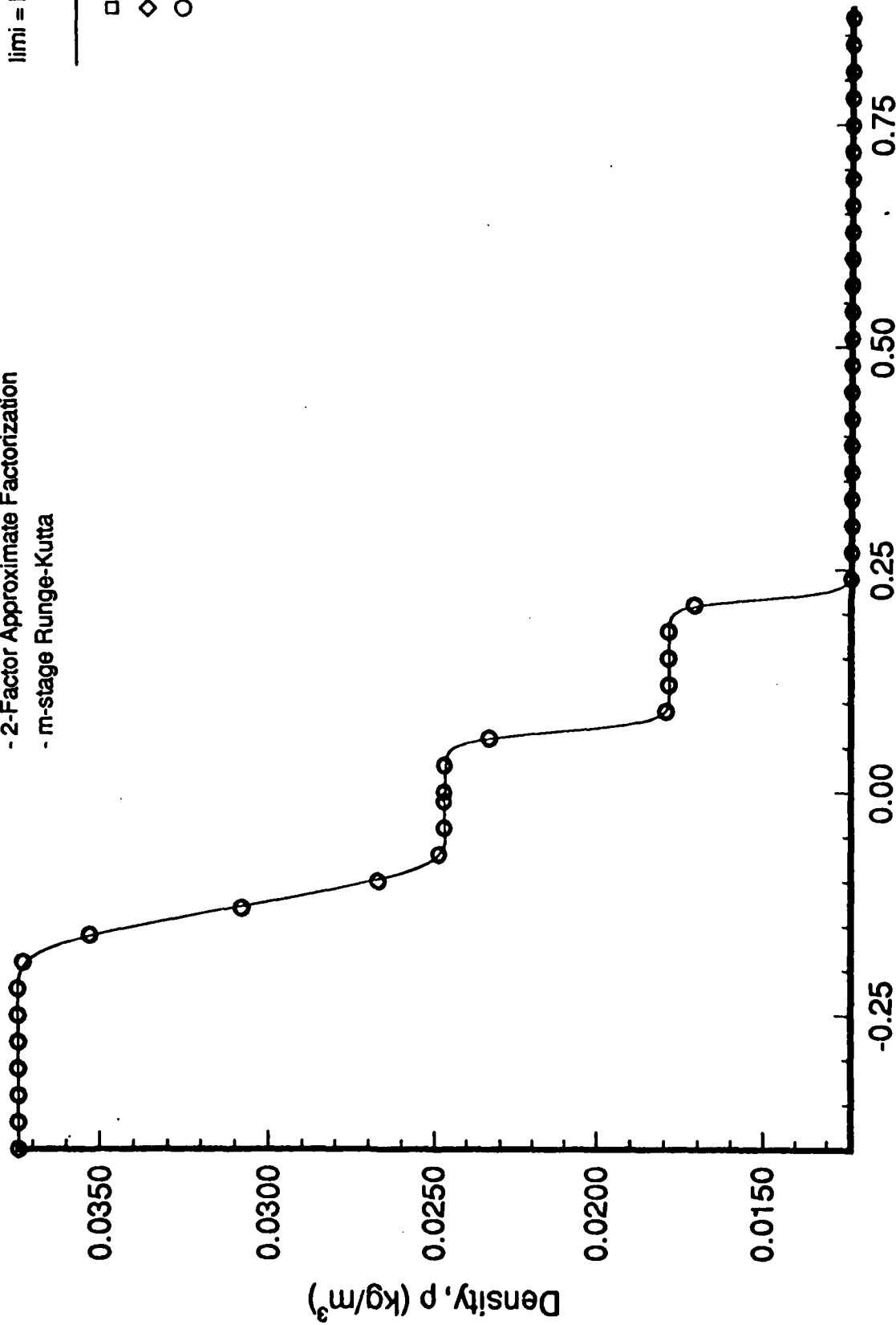
2 stg

◇

4 stg

○

8 stg



Centerline distance (m)

Figure 5

Density variation along the centerline of the Shock Tube

Comparison for varying Δt

Elapsed time = 5.0E-4 s
invfixi = invfixj = 3
rkapi = rkapij = 1/3
limi = limj = 3

○ 0.5E-6 s
— 1.0E-6 s
◇ 2.0E-6 s

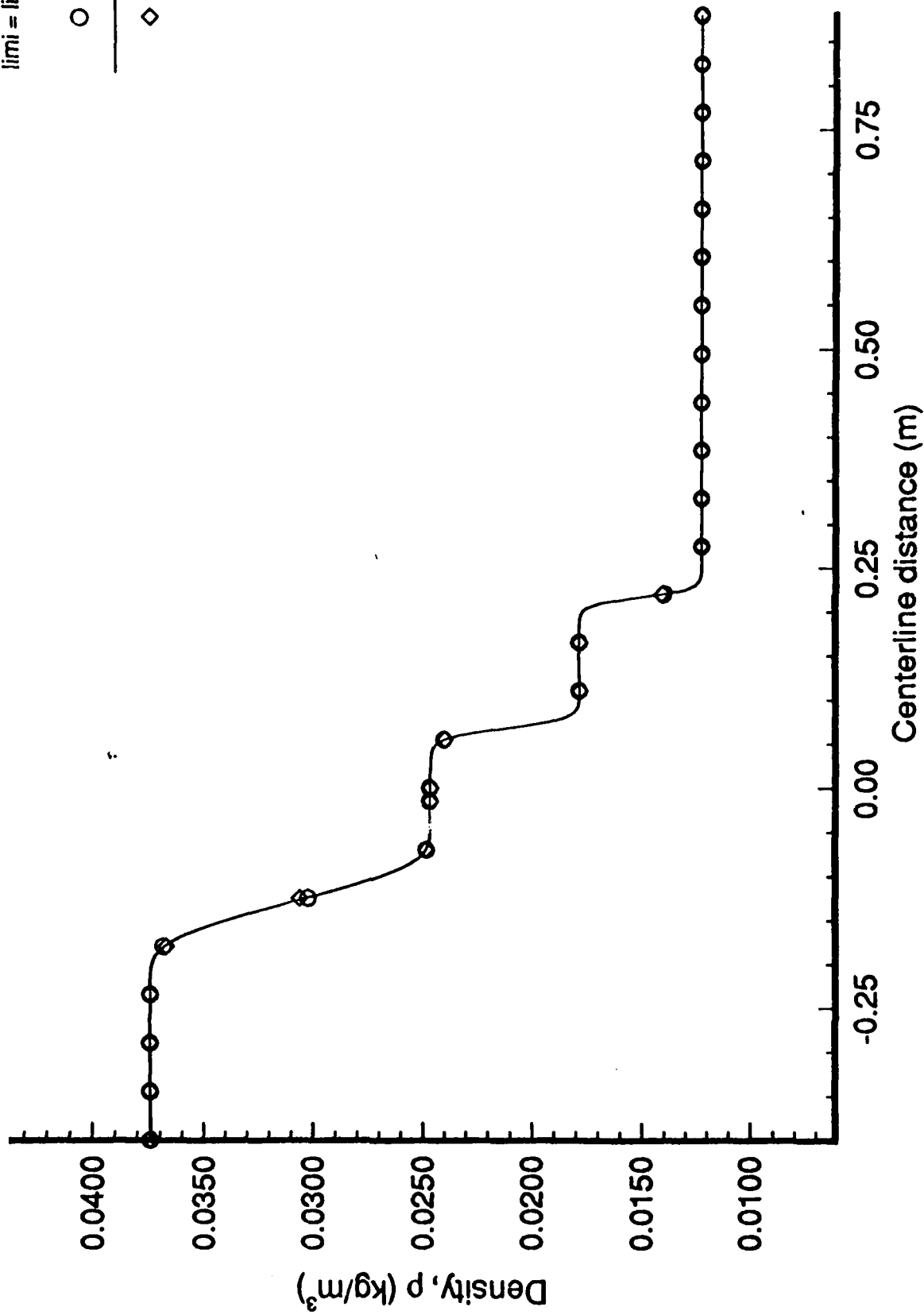


Figure 6

calculation was run at a very low CFL number (0.20), and agreement is excellent. The time step was also varied to establish the solution independence over equivalent periods of time. Figure 6 presents the density profile at the same elapsed time (.5 ms) using three different time steps, and agreement is excellent. Studies were also done comparing Van Leer Flux Vector Splitting and Roe Flux Difference splitting algorithms, which produced nearly identical time-accurate results.

Because accurate resolution of the shock in this time-accurate problem is of importance, substantial work was invested in investigating the effect of different limiters in resolving the shock structure. Figure 7 shows the density near the shock in the tube, with Van Albada and Min-Mod limiters, the last of which gave sharper resolution. Similar comparisons were done for both the expansion wave front and contact surface, shown in Figures 8 and 9.

The GASP time-accurate solution was also compared to a completely independent Flux-Corrected Transport (FCT) solution, at an elapsed time of 0.951 ms (where the FCT data was available). Figures 10-13 show the comparison between density, velocity, temperature, and pressure for the two independent codes, respectively. Once again, agreement was excellent. Finally, for comparison, a viscous solution was run in the shock tube; it compared favorably with the inviscid results and demonstrated suitable time-accuracy.

To validate time accuracy for external flows, GASP was used to calculate properties over the classic 24-degree wedge solution of Holden at Mach 14.1 and Reynolds number 2.36×10^5 . This geometry and the associated data has been used in the past to validate many other codes.¹, and contains features which will be characteristic of a hypersonic inlet ramp. A grid was generated with 121 x 61 points over a 0.439 m-long wedge surface, as is depicted in Figure 14.

¹Rudy, D., Thomas, L., Kumar, A., Gnoffo, P., and Chakravarthy, S., "A Validation Study of Four Navier-Stokes Codes for High Speed Flows," AIAA 89-1838, AIAA 20th Fluid Dynamics, Plasmadynamics, and Lasers Conference Buffalo, N.Y. June 1989.

Elapsed time = 5.0E-4 s
invfixi = invfixj = 3
rkapi = rkapij = 1/3

Density variation along the centerline of the Shock Tube

Comparison of two limiters near the expansion wave

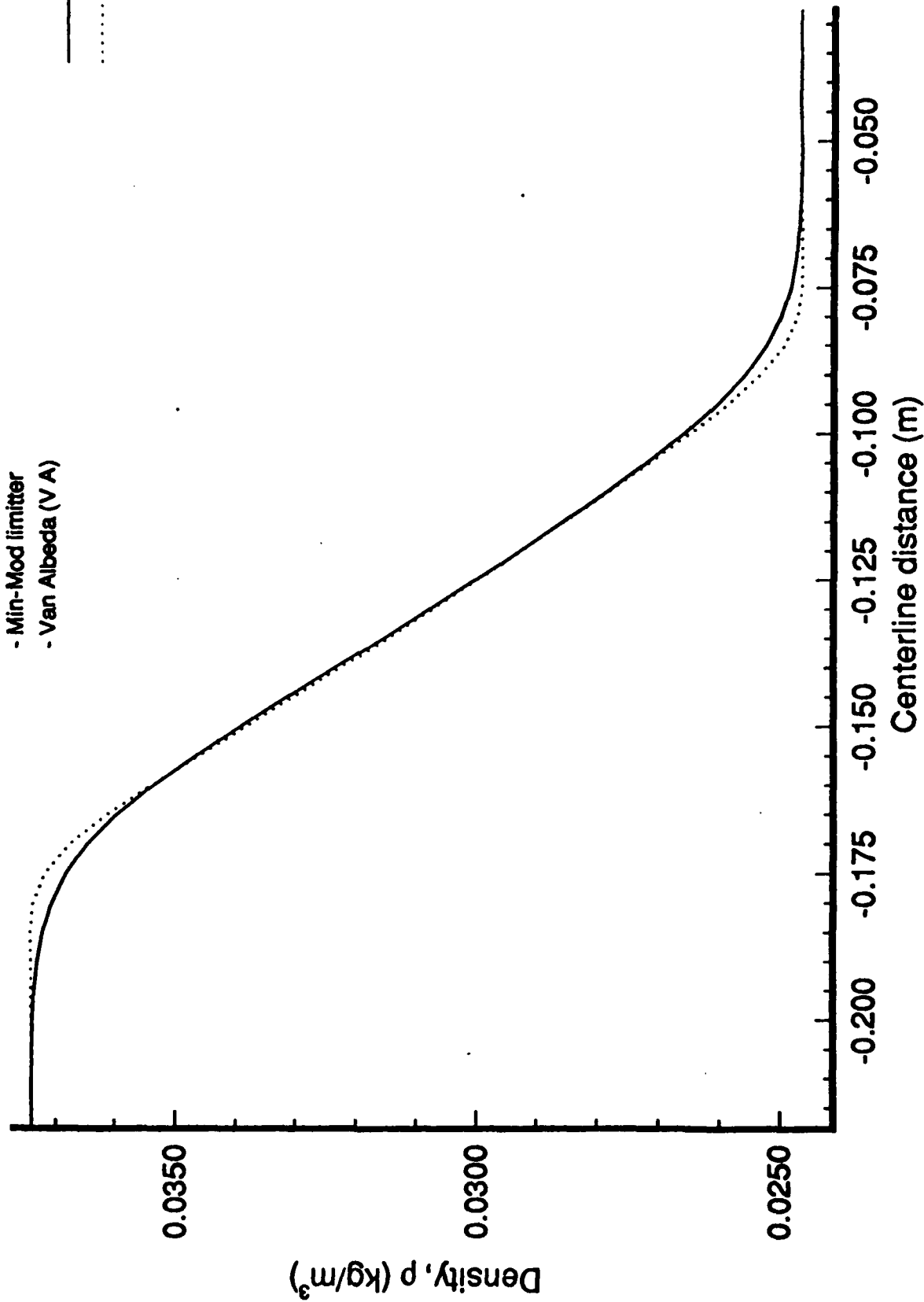


Figure 8

Elapsed time = 5.0E-4 s
invfixi = invfixj = 3
rkapi = rkapij = 1/3

Density variation along the centerline of the Shock Tube

Comparison of two limiters near the contact surface

- Min-Mod limiter
- Van Albeda (V A)

— V A
..... Min-Mod

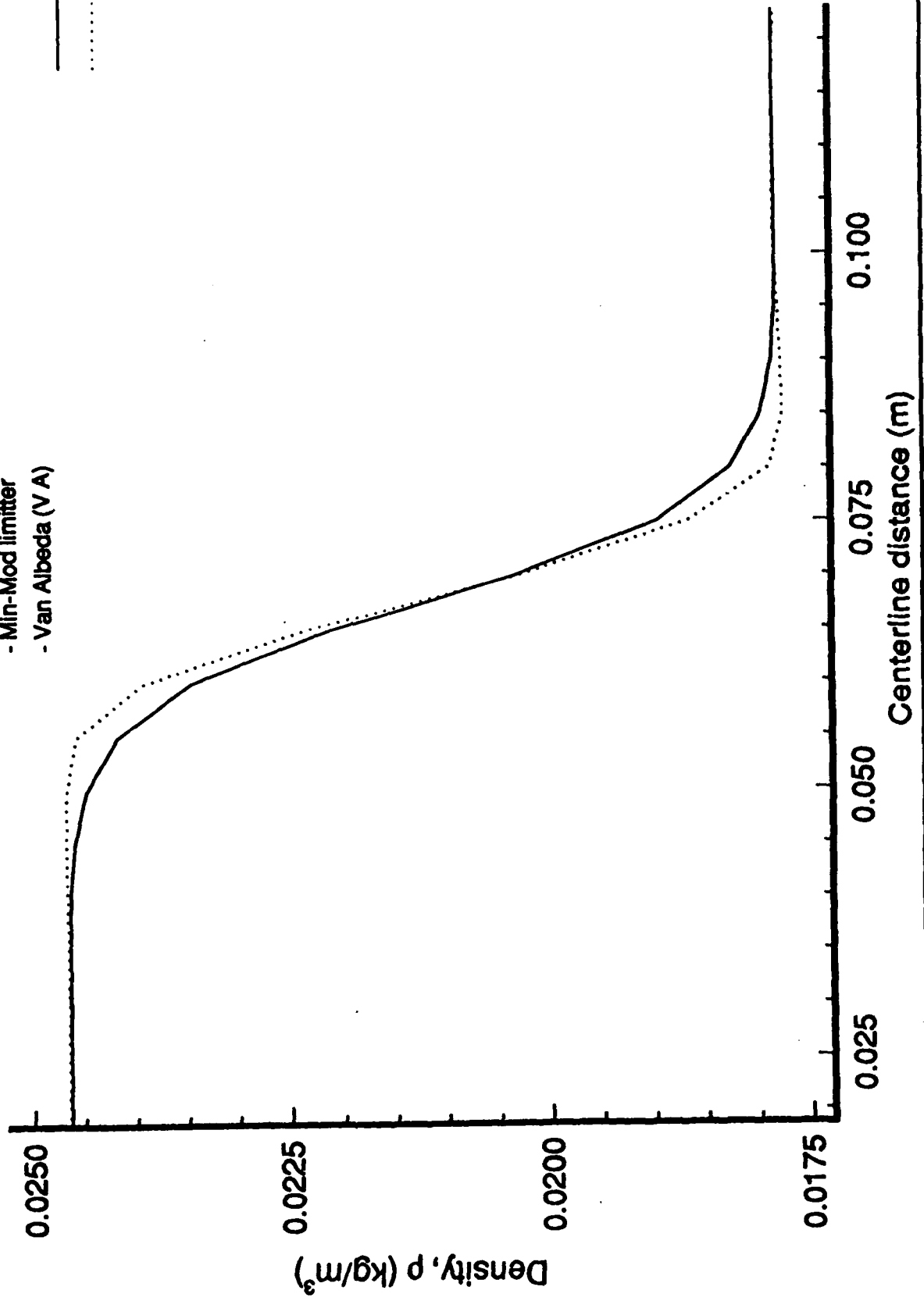


Figure 9

Density variation along the centerline of the Shock Tube

A comparison between two different algorithms

- Roe's Flux Difference Splitting scheme
- Flux-Corrected Transport (FCT) Scheme

(FCT data from Yvette S. Weber)

..... FCT
—— Roe

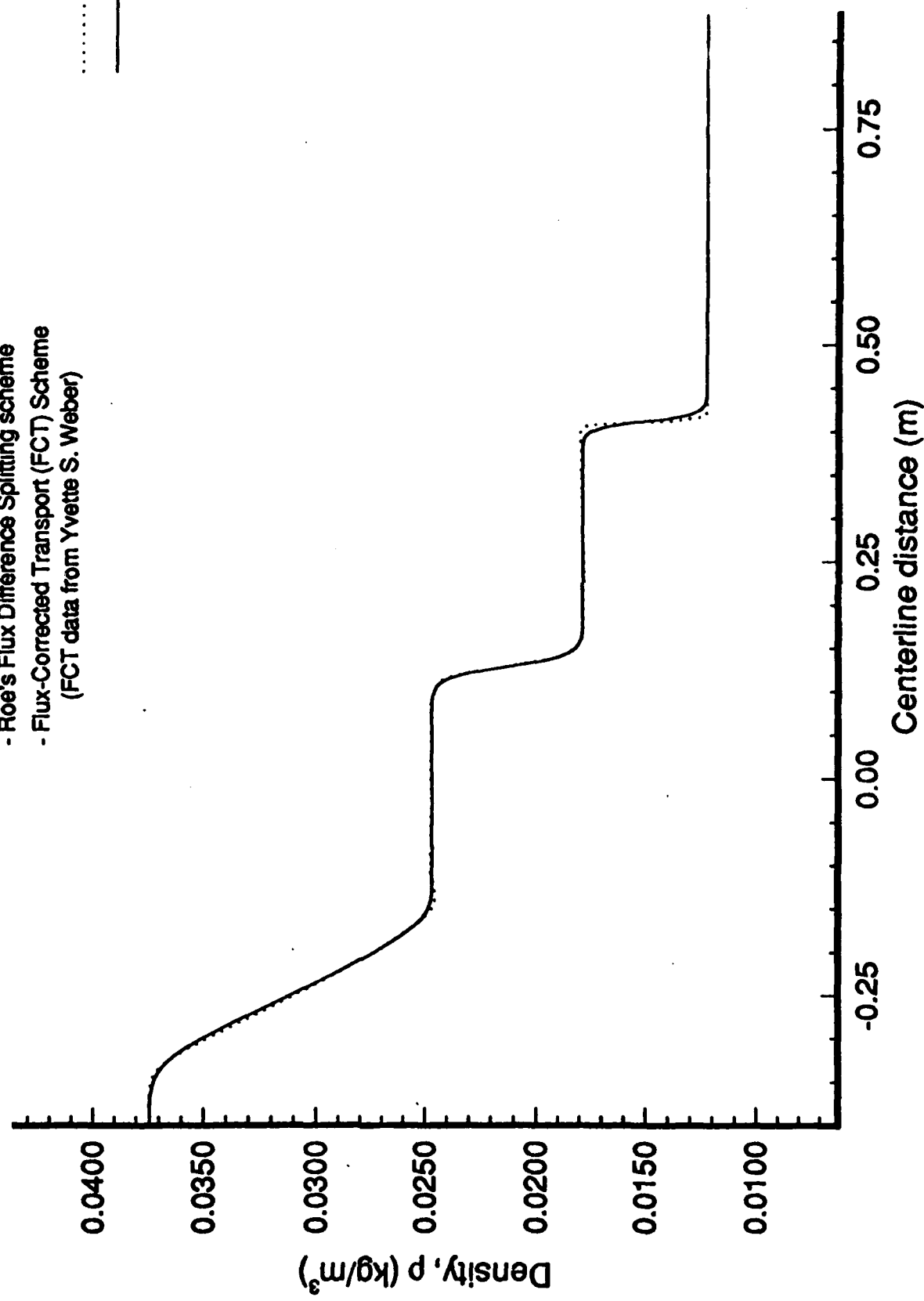


Figure 10

Velocity(u) variation along the centerline of the Shock Tube

Elapsed time = 9.51E-4 s

A comparison between two different algorithms
- Roe's Flux Difference Splitting scheme
- Flux-Corrected Transport (FCT) Scheme
(FCT data from Yvette S. Weber)

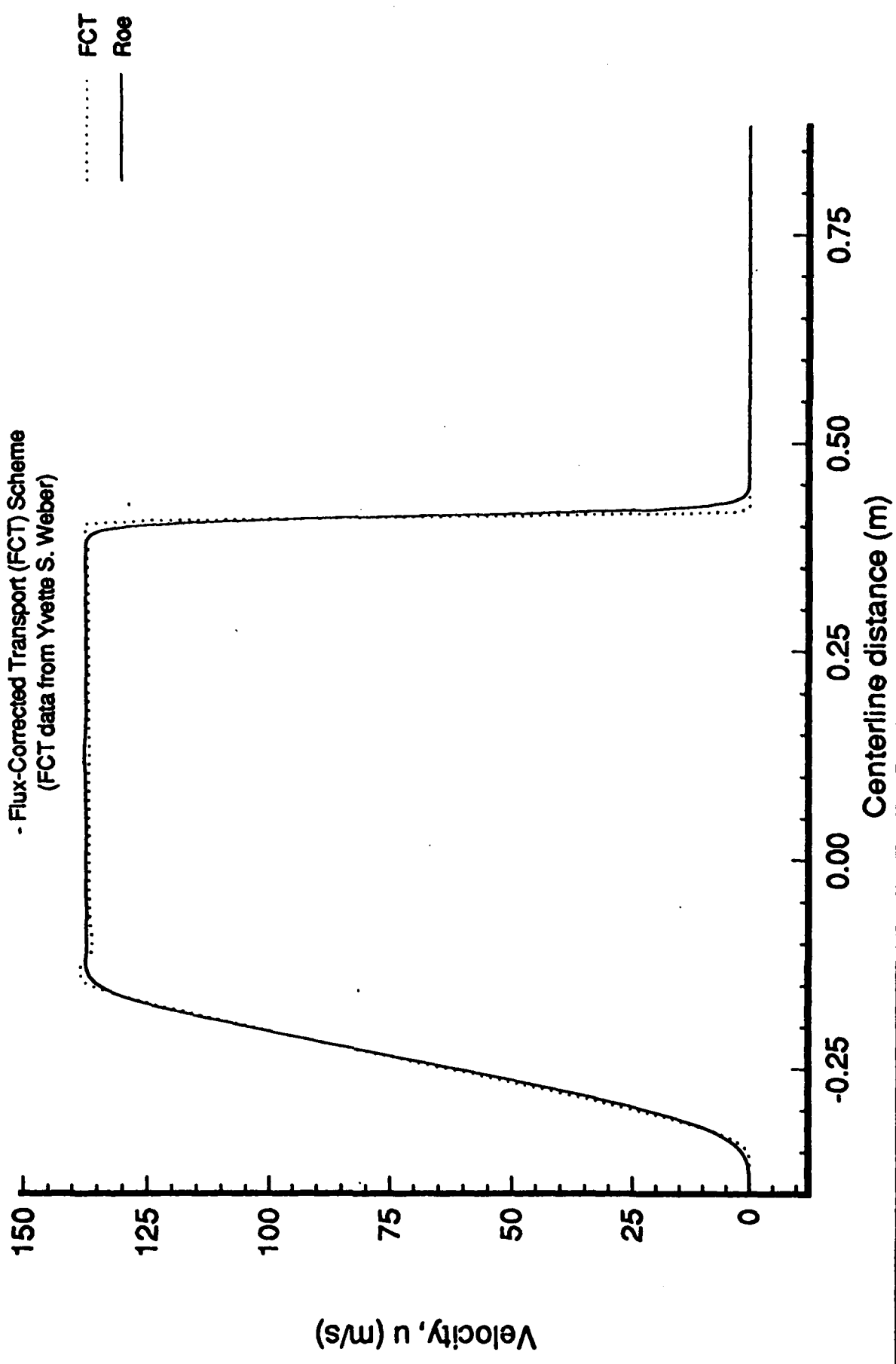


Figure 11

Temperature variation along the centerline of the Shock Tube

Elapsed time = 9.51E-4 s

A comparison between two different algorithms

- Roe's Flux Difference Splitting scheme
- Flux-Corrected Transport (FCT) Scheme
(FCT data from Yvette S. Weber)

..... FCT
—— Roe

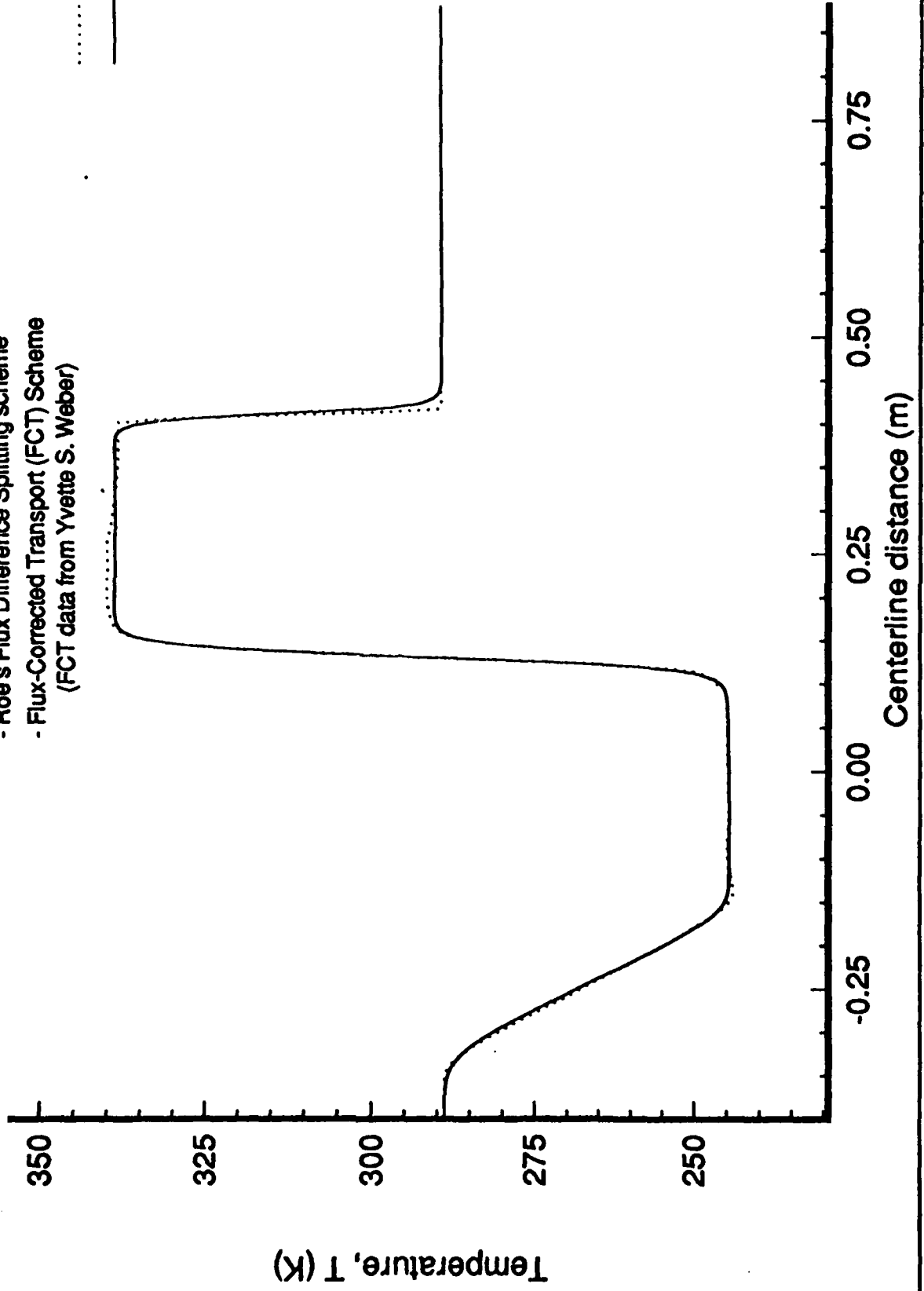


Figure 12

Pressure variation along the centerline of the Shock Tube

Elapsed time = 9.51E-4 s

A comparison between two different algorithms

- Roe's Flux Difference Splitting scheme
- Flux-Corrected Transport (FCT) Scheme
(FCT data from Yvette S. Weber)

..... FCT
—— Roe

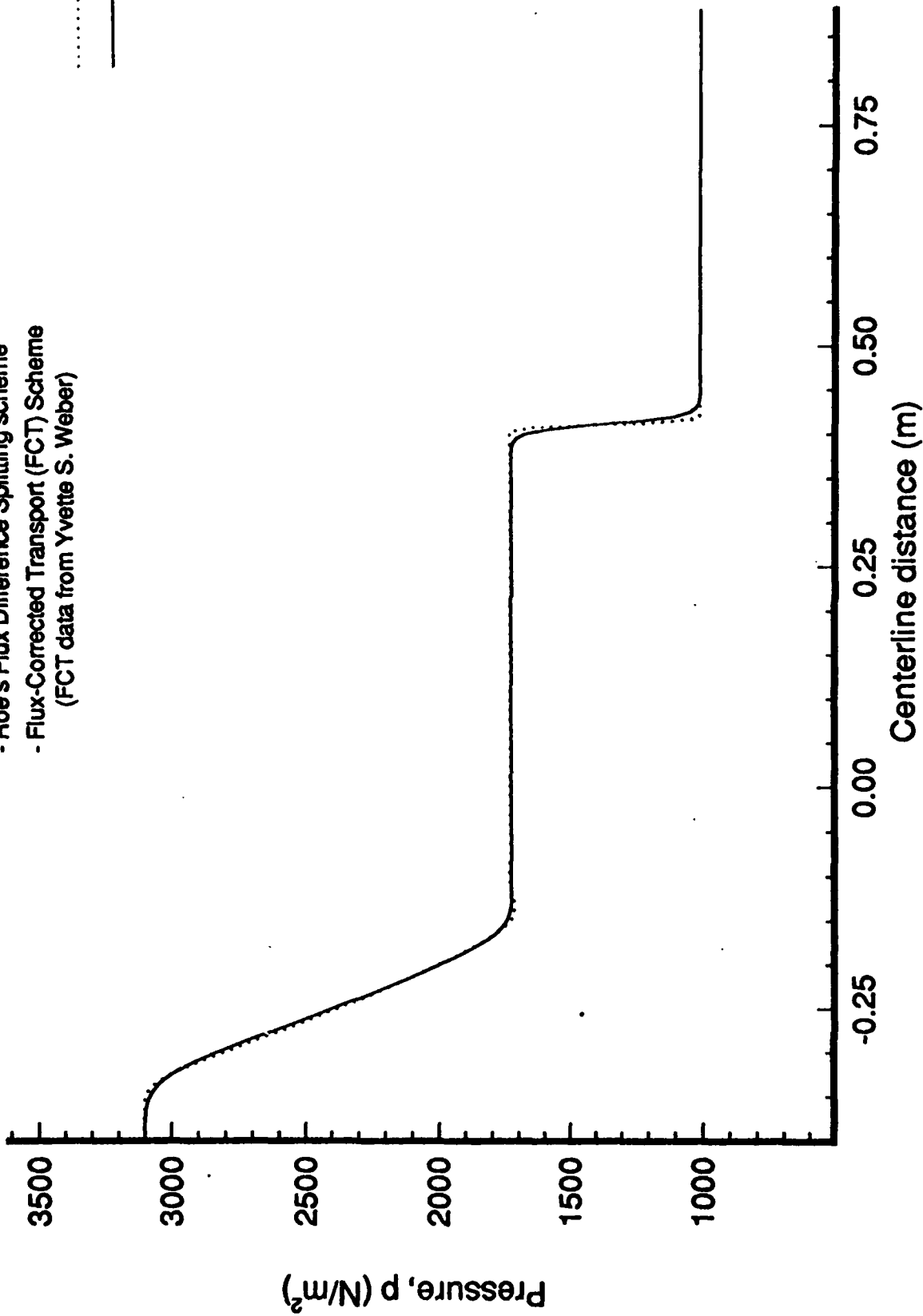


Figure 13

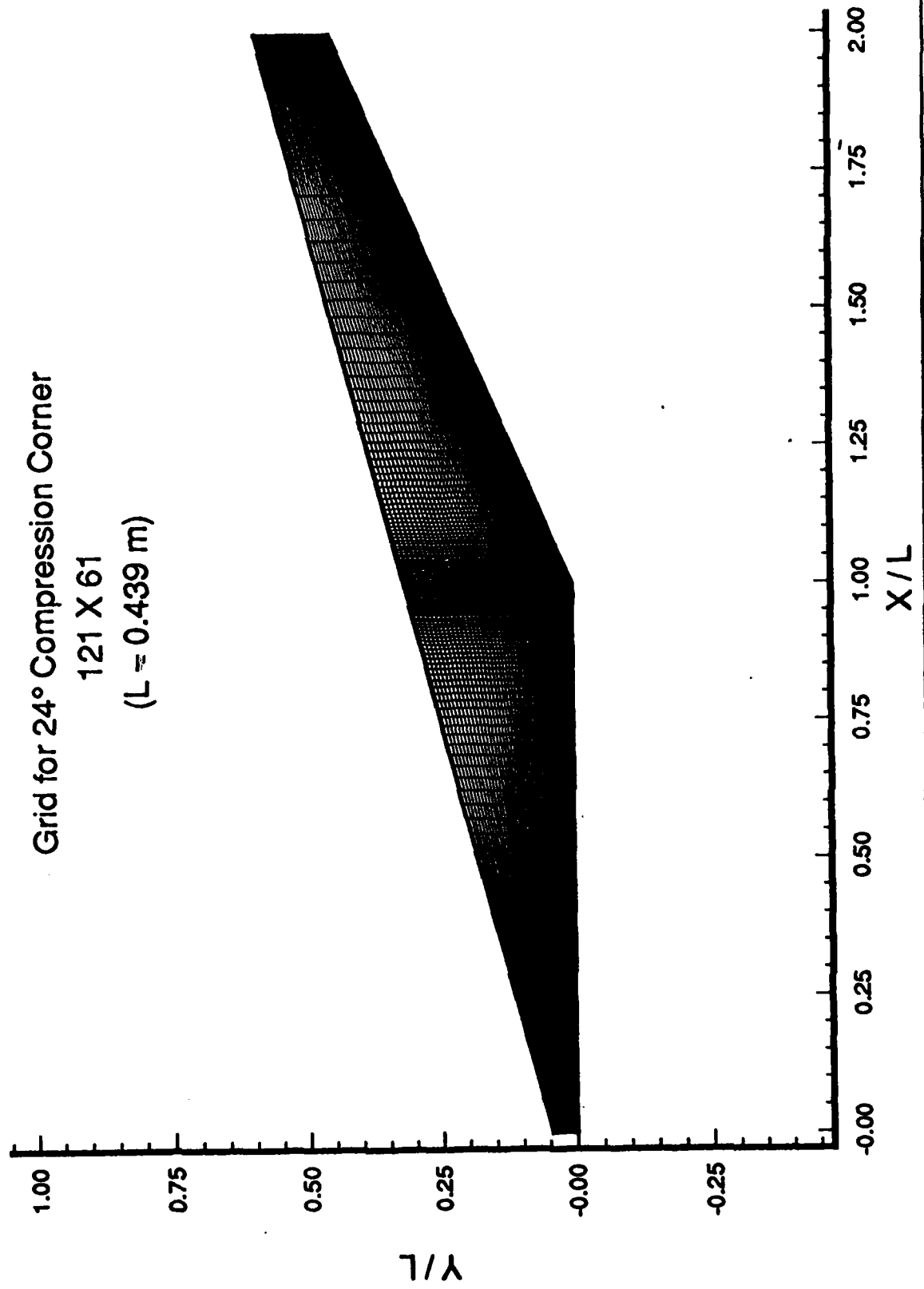


Figure 14

Figures 15, 16, and 17 show density, pressure, and Mach number contours at times 1 ms, 3 ms, and 6 ms, respectively. Figures 18 and 19 show velocity vector plots of the wedge flowfield at times 1 ms, 2 ms, and 5 and 6 ms. The separated region is captured, and grows through the calculation, in exact agreement with the experimental results. Figure 20 shows the time history of the surface pressure, which compares very well with the experimental data. This simple case is obviously far removed from the fully three-dimensional inlet, yet it serves to provide confidence in the code's ability to handle that flow with time accuracy.

Geometry Selection:

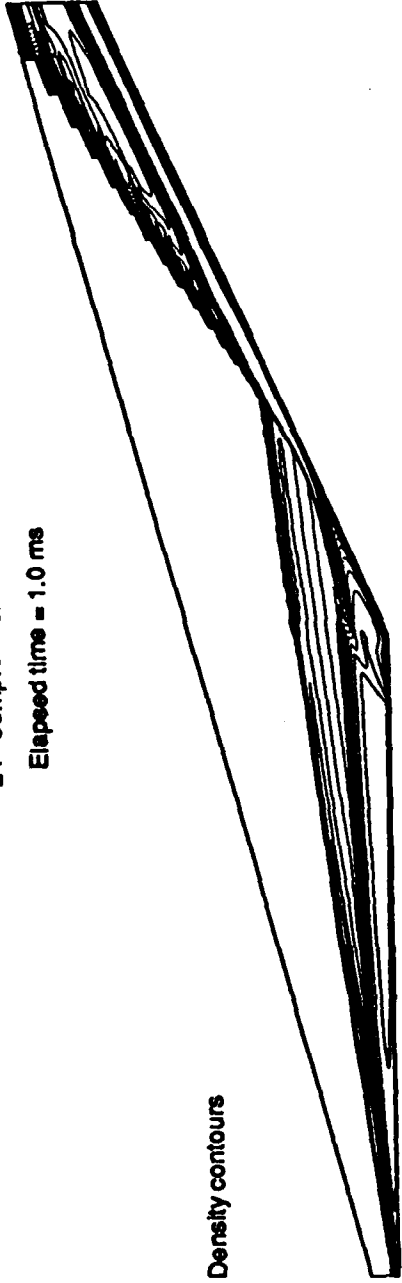
An important element of this work was the selection of a suitable generic scramjet inlet geometry with realistic, three-dimensional effects, and with the potential for application to a realistic engine system. This work is not tied to any particular engine design or vehicle concept per se, so it was desired to find a geometry which would exhibit physical results of interest, while at the same time being as simple as possible to generate a computational grid structure.

For this work, two baseline geometries were selected. Although this project was directed towards a fully-three-dimensional solution, initial studies and validation were done in two dimensions. Subsequent studies used the fully three-dimensional geometry.

Substantial efforts were devoted to selecting the best way to represent a three-dimensional inlet in two dimensions. The simplest solution would be to extract inlet geometries which are two-dimensional slices from the three-dimensional form. However, that does not provide comparable thermodynamic or velocity conditions. For instance, if the three-dimensional inlet has sidewall compression, a two-dimensional slice will have less compression, and therefore not reproduce a two-dimensional slice of the three-dimensional flow. As a result, numerical tests will be done on two separate sets of inlets, one for two-dimensions and another for three. Initial work has been done on a two-dimensional configuration, for code development and

24° Compression Corner
Elapsed time = 1.0 ms

Density contours



Pressure contours



Mach contours



Figure 15

24° Compression Corner
Elapsed time = 3.0 ms

Density contours



Pressure contours



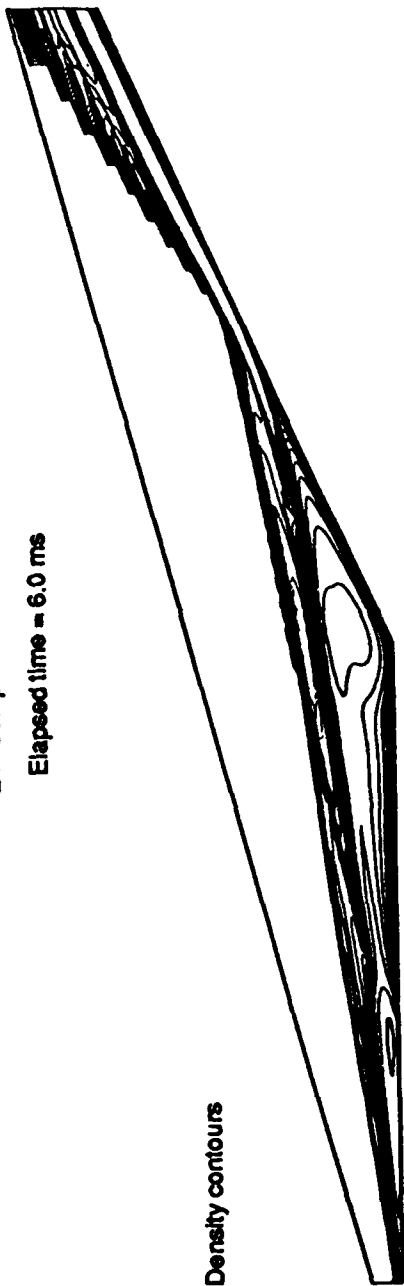
Mach contours



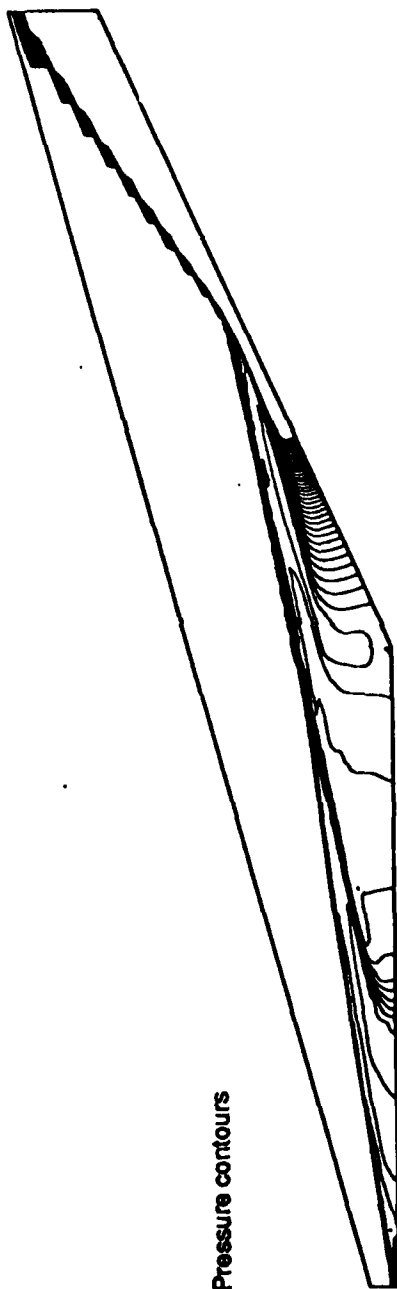
Figure 16

24° Compression Corner
Elapsed time = 6.0 ms

Density contours



Pressure contours



Mach contours



Figure 17

24° Compression Corner
Velocity vector showing extent of separated region

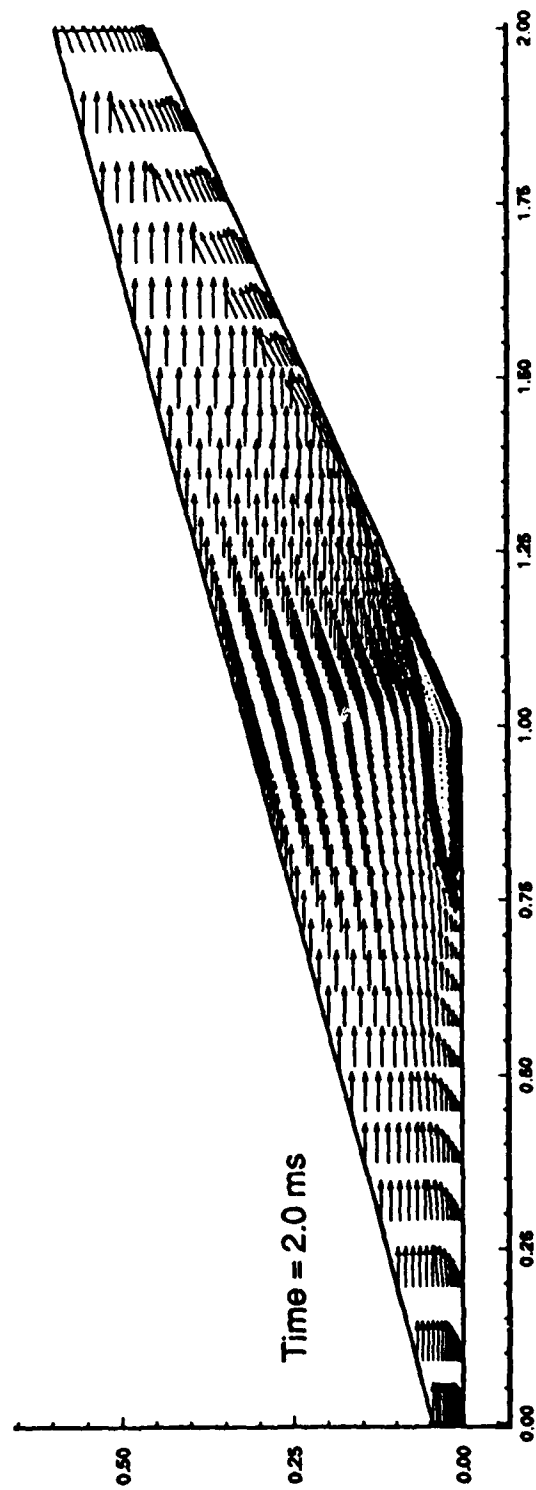
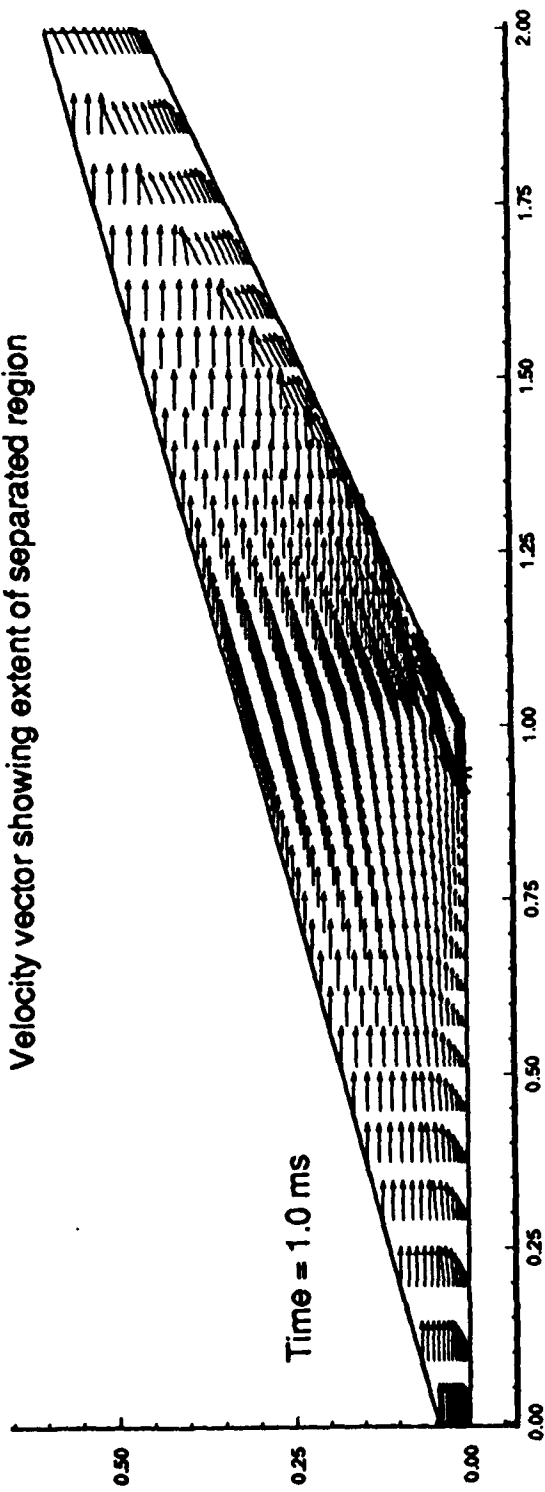


Figure 18

24° Compression Corner
Velocity vector showing extent of separated region

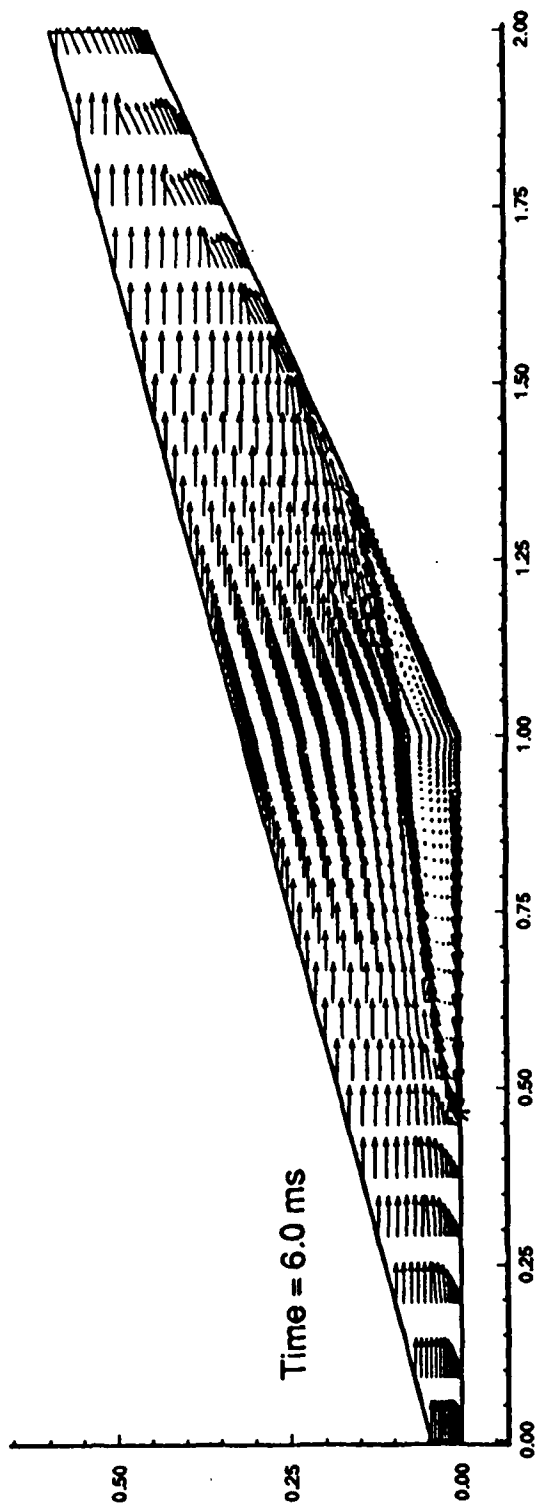
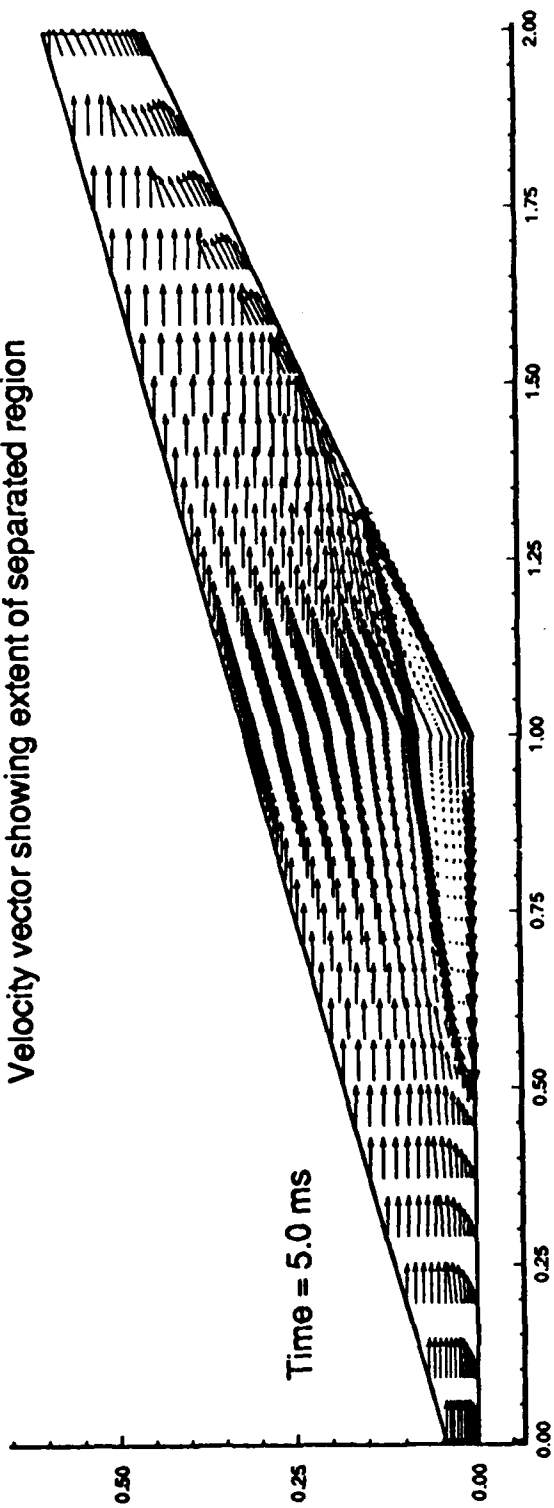


Figure 19

24° Compression Corner
Time history of surface pressure

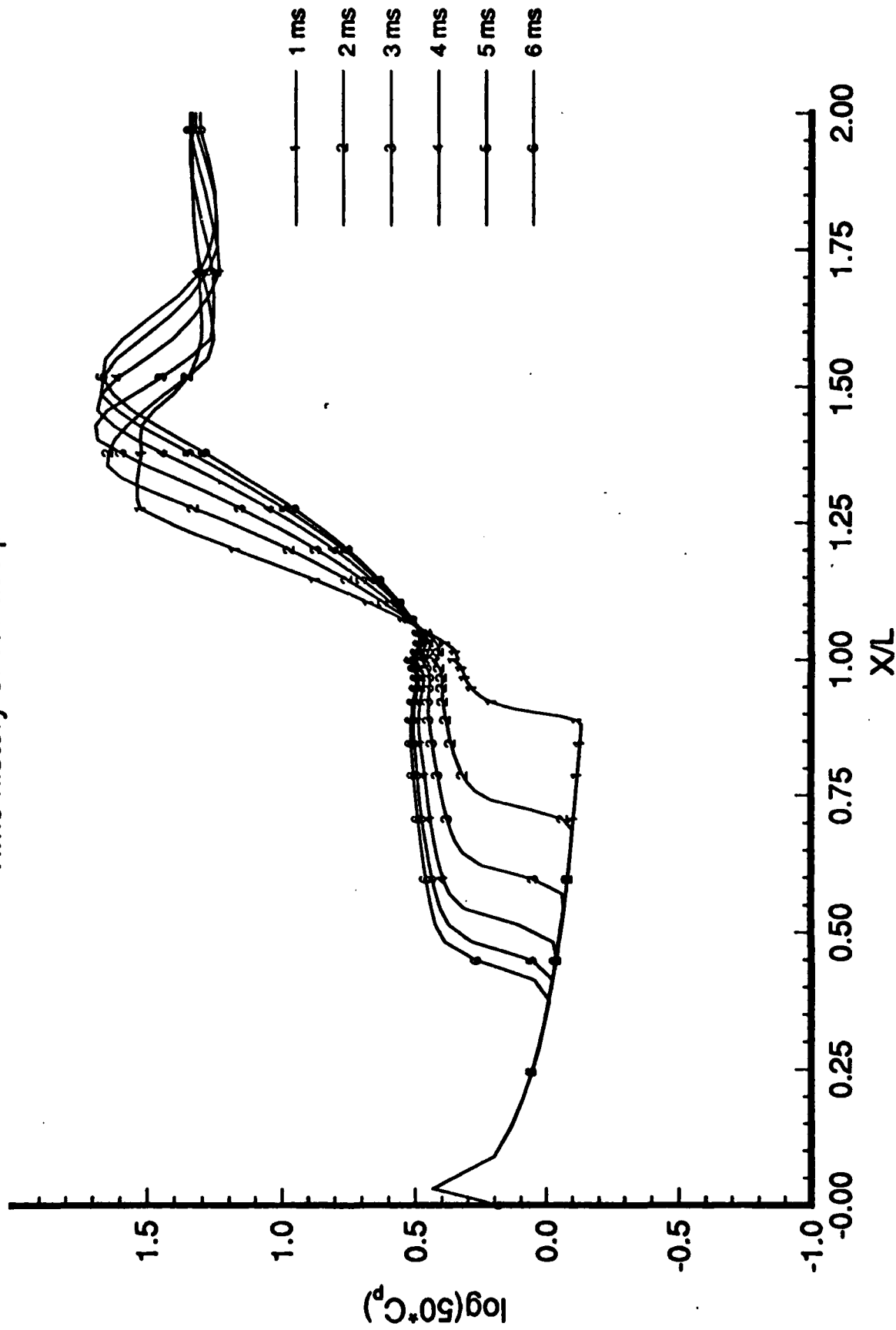


Figure 20

validation purposes. Subsequent studies will be conducted on three-dimensional geometries.

For the two-dimensional work, two separate geometries were selected. The first is the Rensselaer Polytechnic Institute generic scramjet model. This model has been tested by Minucci and Nagamatsu, across the Mach number range to 18, and so data is available for comparison². Another geometry was designed in-house to provide shock-on-lip flow conditions at design, to minimize shock-boundary layer interactions inside the combustor channel. This shape was adopted because the RPI model does not provide such operating conditions, and the computational solutions were exhibiting extensive separated regions on the combustor walls which were deemed unrealistic for practical engine designs.

Since the ultimate goal of this program was to study unstart physics with a fully-three-dimensional geometry, the NASA Langley "Parametric Scramjet Module" was selected for the bulk of these studies, as pictured in Figure 21. This design has several advantages, primarily in that there is unclassified experimental data available for code validation (though not including unstarts), and it is fully three-dimensional, including the use of sidewall compression ramps.³ This design also includes injection struts in the main flow. It was hoped that such struts could eventually be included in the computational grid, but that was not achieved during the reporting period.

Grid Generation

²Minucci, M., and Nagamatsu, H., "Experimental Investigation of a 2-D Scramjet Inlet at Mach Numbers of 8 to 18 and Stagnation Temperatures of 4,100K," AIAA 91-0013, 29th Aerospace Sciences Meeting, Reno, Nev. January 1990.

³Trexler, C., and Souders, S., "Design and Performance at a Local Mach Number of 6 of an Inlet for an Integrated Scramjet Concept," NASA Technical Note TN D-7944, August 1975.

(3D) || Print || scram.wbs.plt || scram.wbs.dat

Scramjet Engine with sweep, $\Lambda = 30.0$ deg
131 X 51 X 31

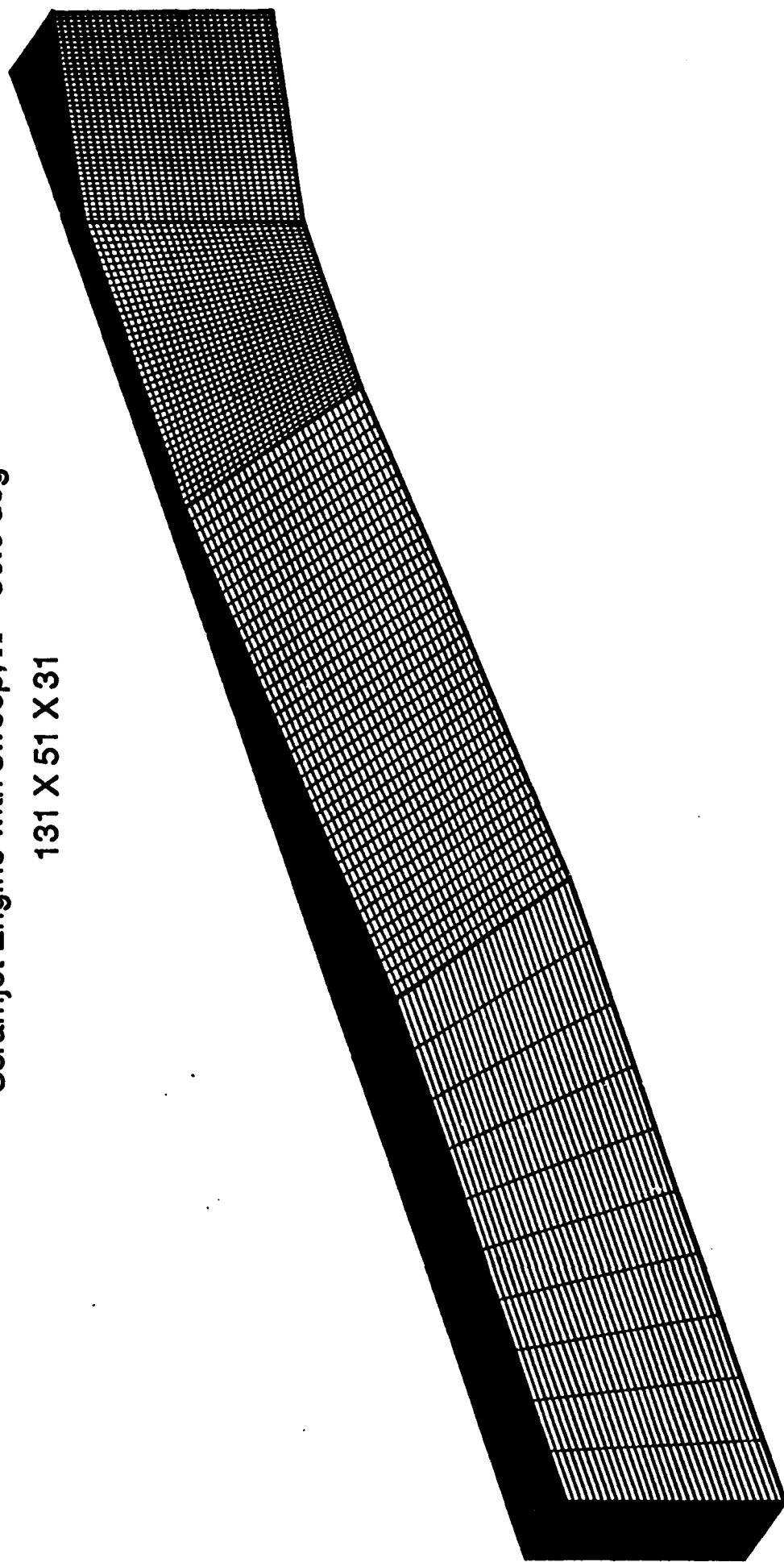


Figure 21

Solid surfaces of a
Scramjet Module with Side-Wall Compression
and Backward Sweep ($\Lambda = 48^\circ$)

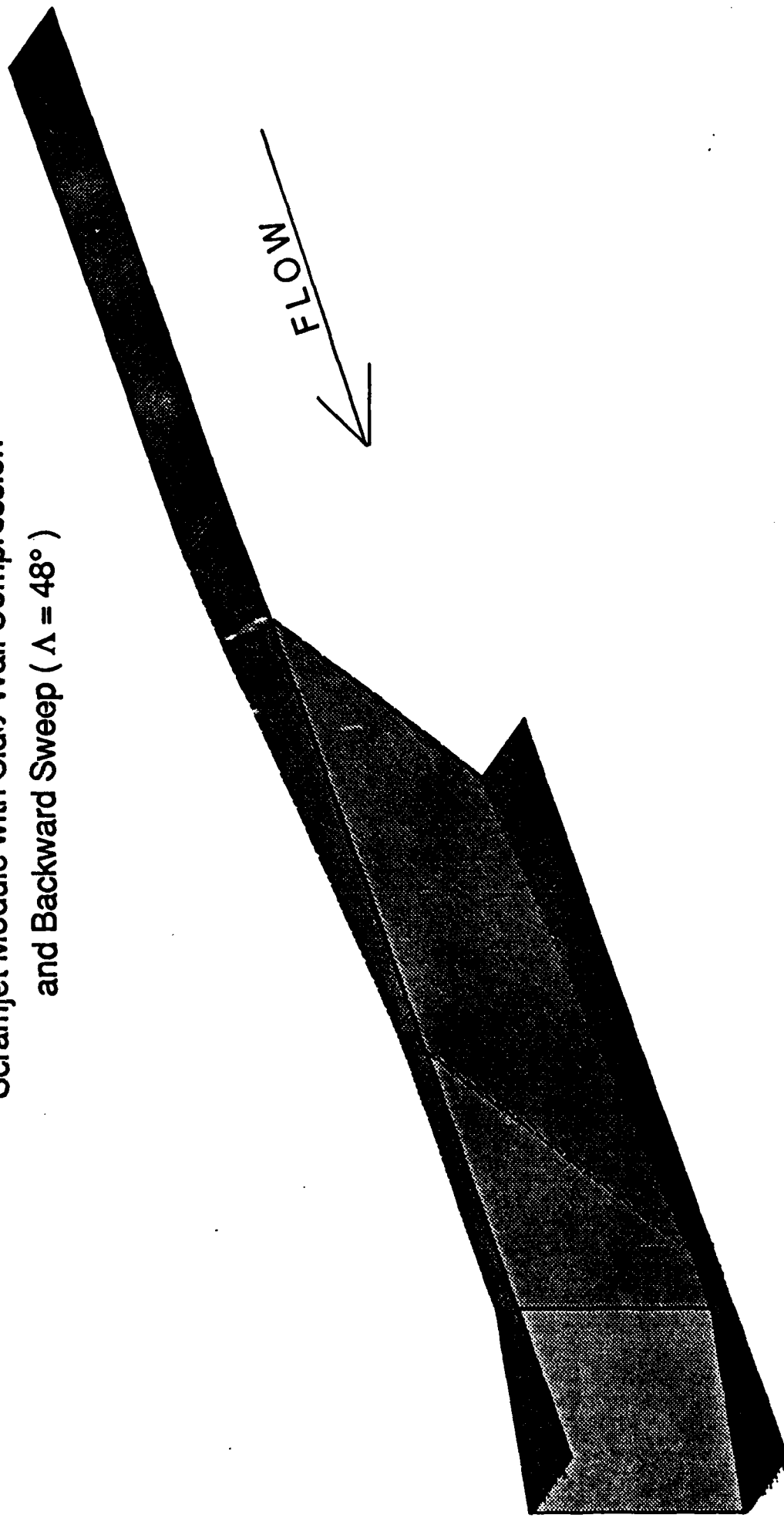
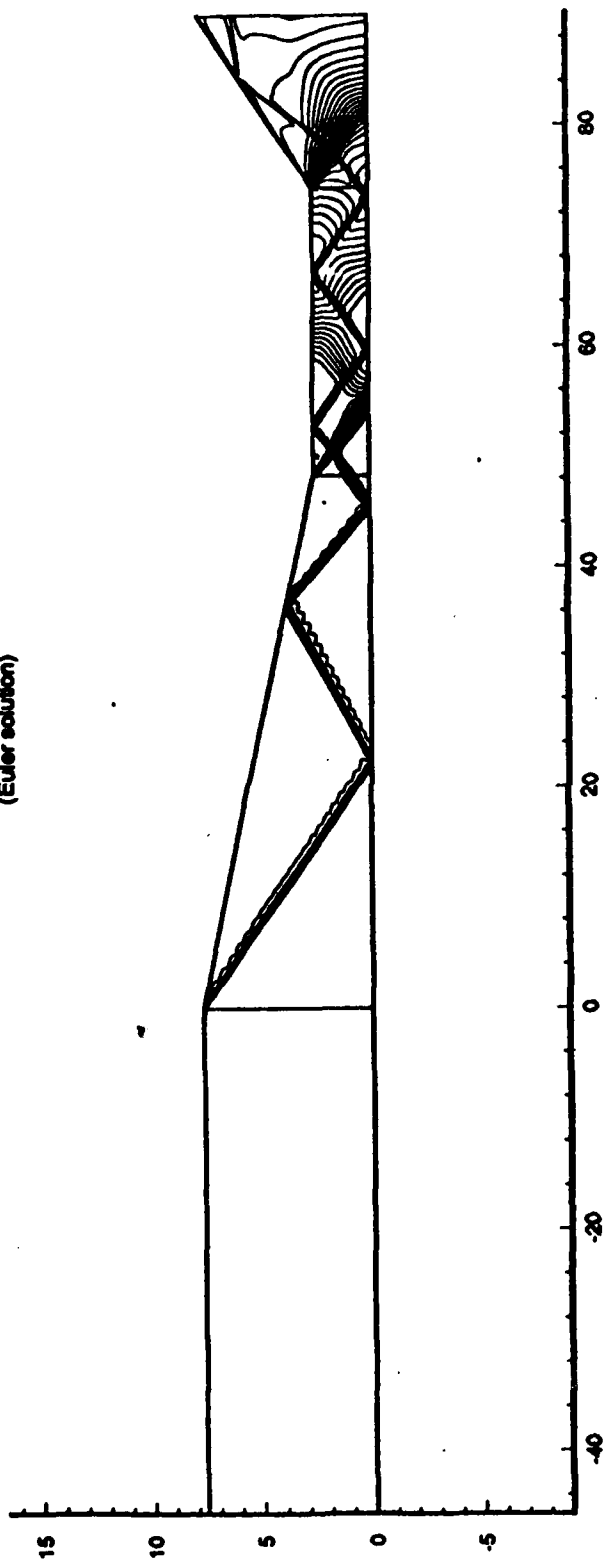
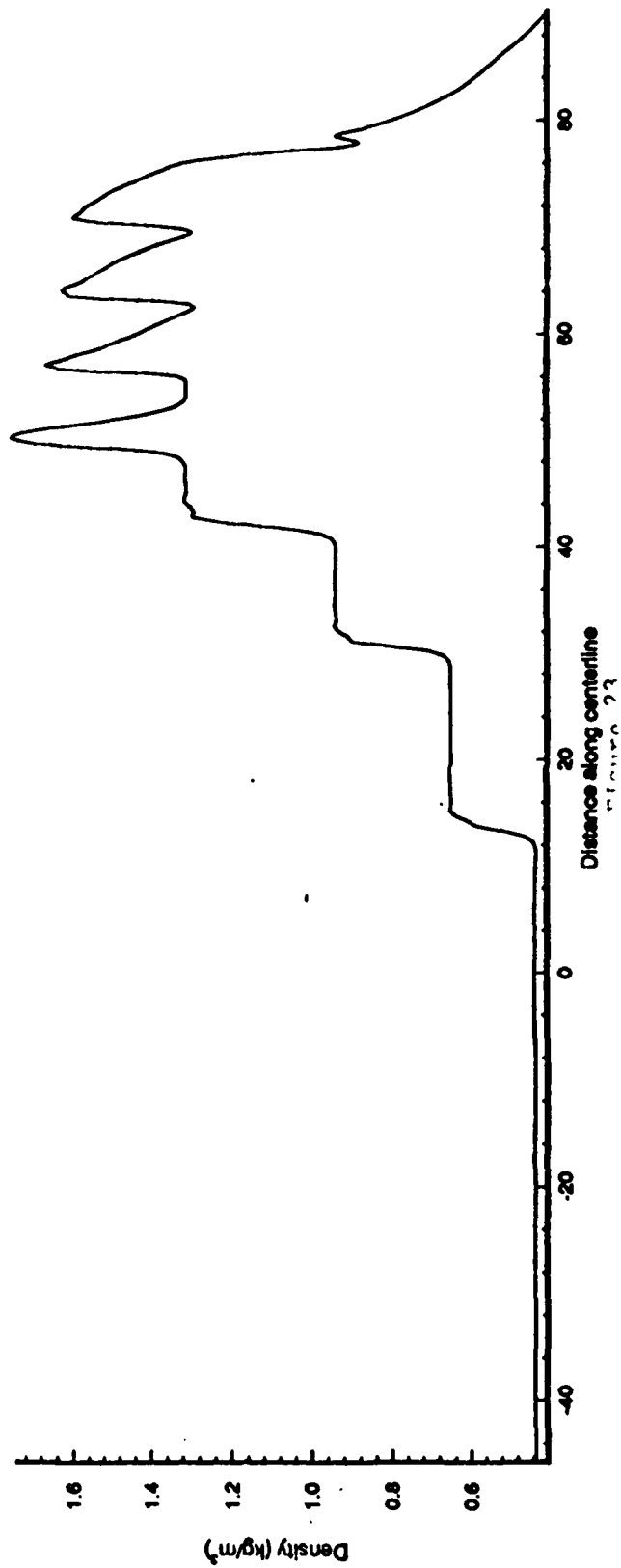


Figure 22

Density contours of a
Mach 4 Flow through a 2D cross-section of a Scramjet Engine
(Euler solution)



Variation of density through centerline of Scramjet



Grid for RPI model

Grid size: 251 x 101

(Note: for clarity only every other point is shown)

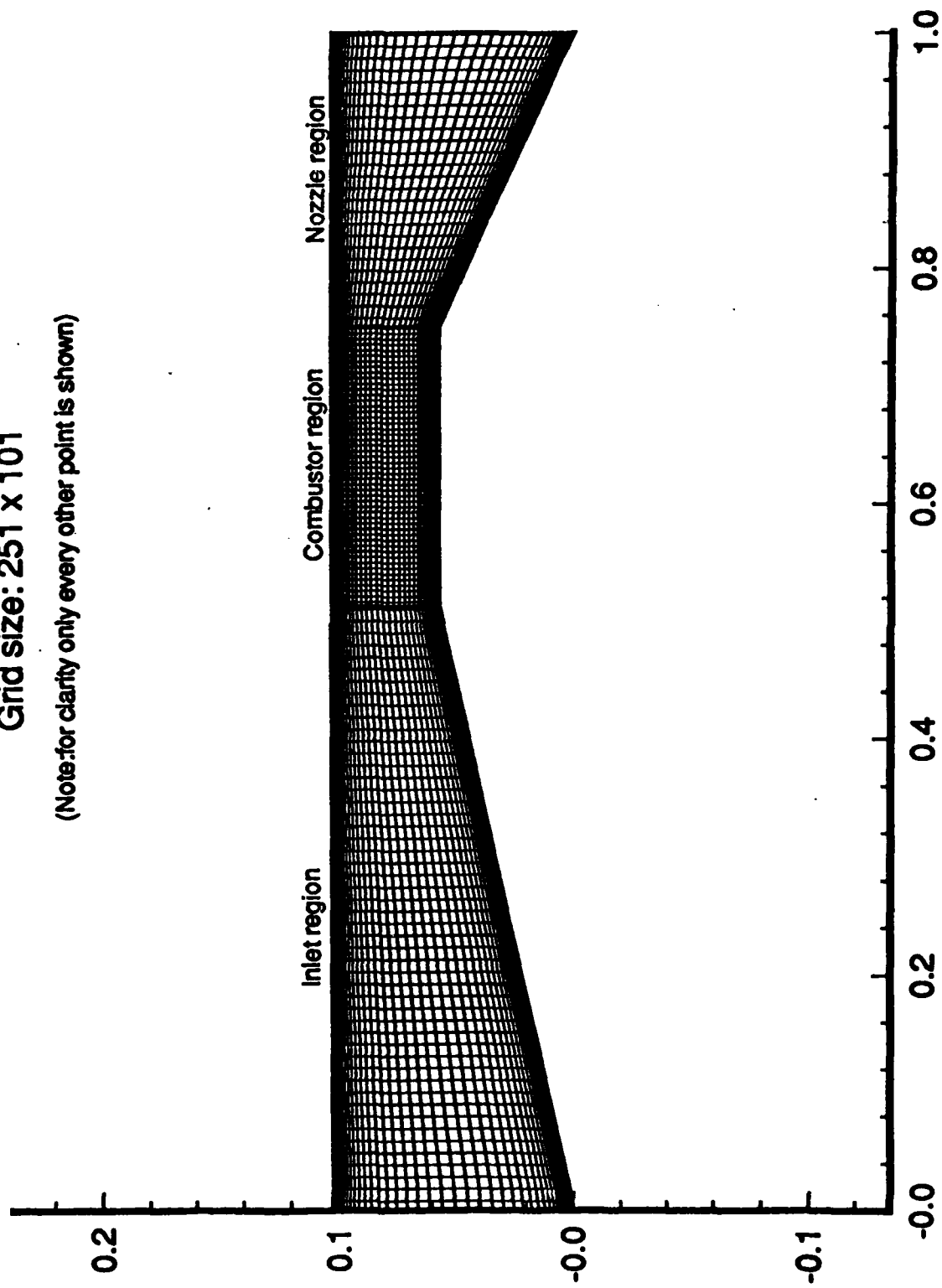
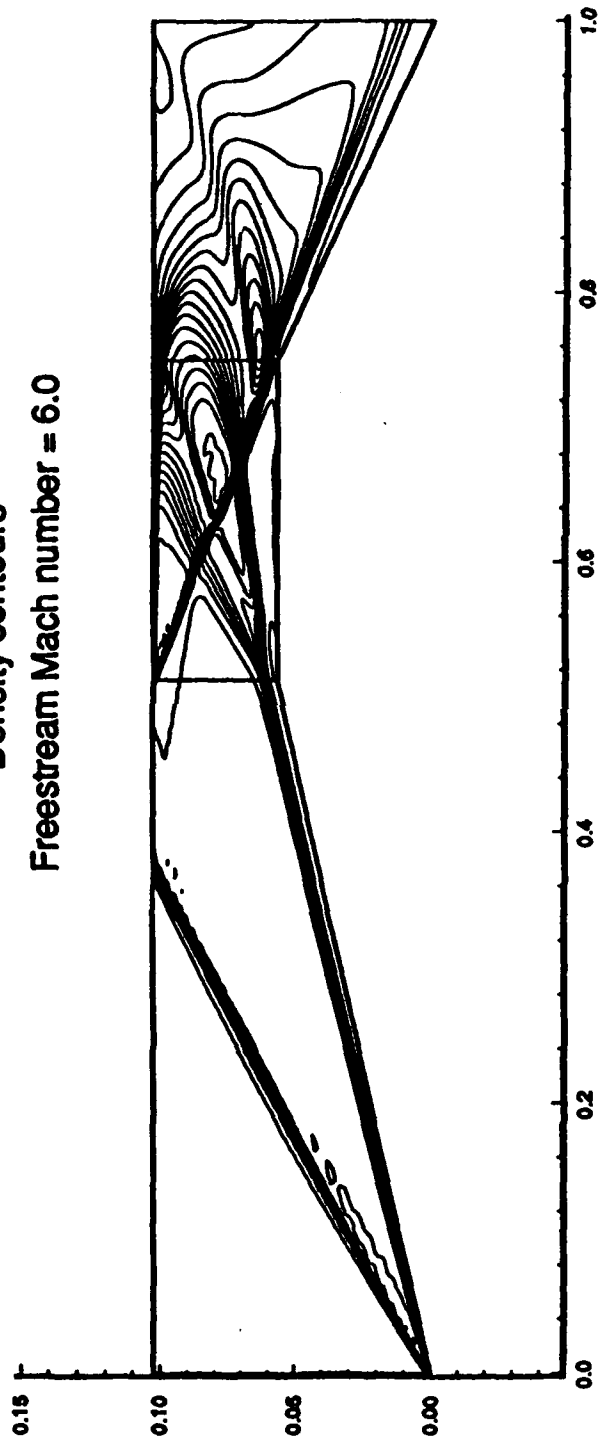


Figure 24

Density contours
Freestream Mach number = 6.0



Mach contours
Freestream Mach number = 6.0

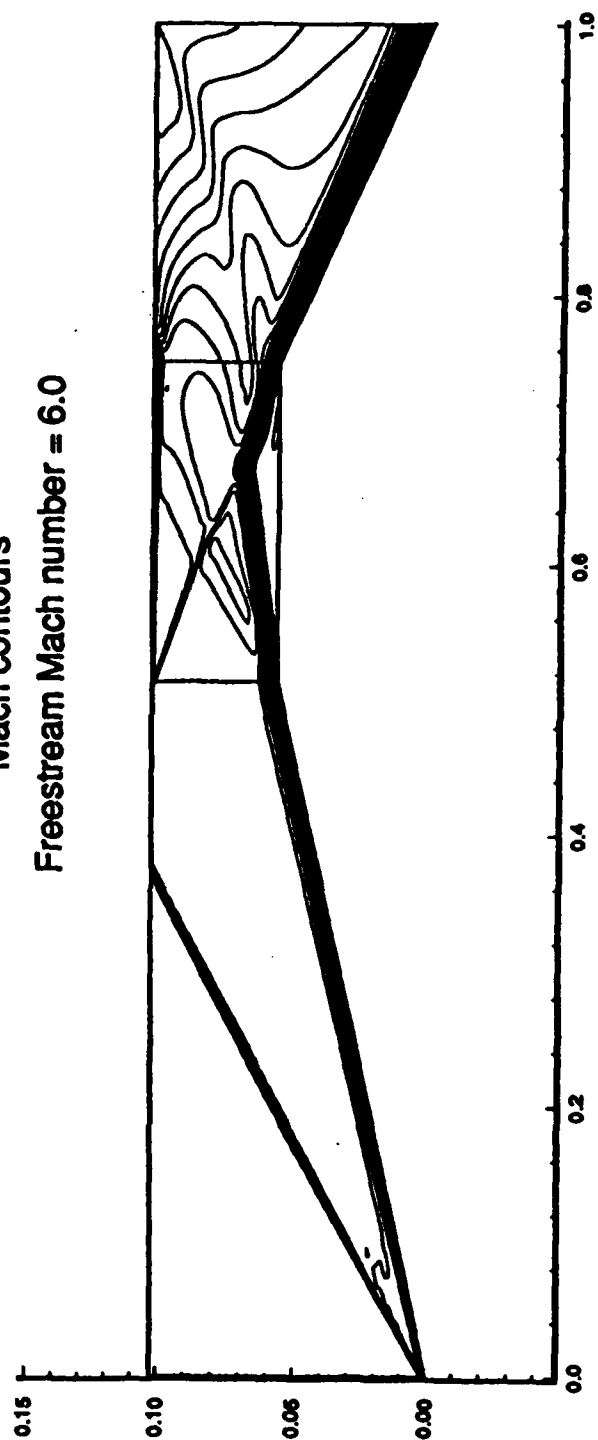


Figure 25

Figure 26 presents the velocity vectors and pressure distribution in the separated region at steady state. All of the features of the shock/boundary layer interaction have been captured correctly. Figure 27 shows the time history of the evolution of the separation region; note the rapid growth of this zone. Corresponding velocity vectors are shown in Figure 28, with snapshots at 1, 1.5, and 2 ms after initial shock impingement. The corresponding density contours are shown in the following Figure 29.

Computational Results

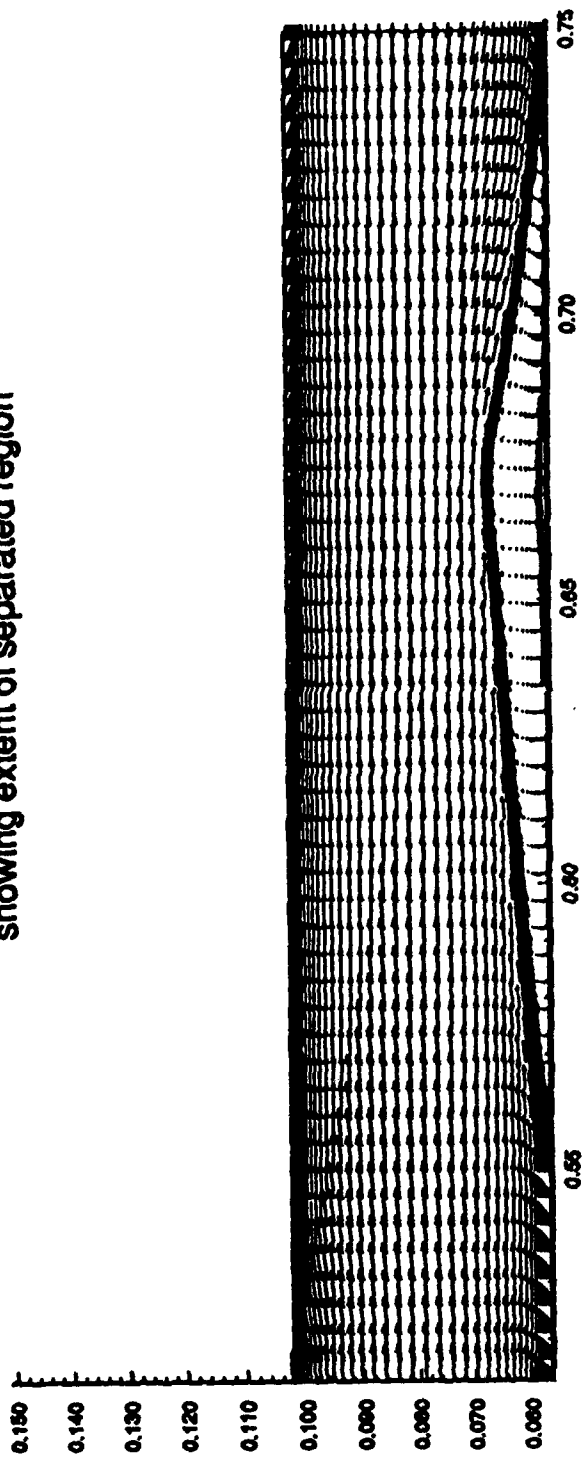
Activities for the second year were focussed on calculations in the chosen 3-D grid, as shown in Figure 30. This is a 41x61x91 3-D grid, with 30-degrees leading edge sweepback. Calculations began with the intention of establishing steady-state solutions at moderate mach number. Figure 31 presents Mach contours calculated with an Euler solution at Mach 6. The fully-three-dimensional shock structure has been captured in this calculation.

Figure 32 presents density contours at the first and last z-axis stations in the scramjet. Temperature contours are shown in Figure 33, also at the first and last z-axis positions. Normalized pressure and density are shown in Figures 33 and 34, where the effect of each shockwave in the engine is apparent. One point of note is the rapid jump in pressure and density corresponding to the second shock reflection in the engine channel, likely source of an adverse shock-boundary layer interaction in a fully-viscous calculation.

The three-dimensional nature of the steady-state Euler solution is demonstrated by Figure 36, which represents the density distribution at the z-axis extreme from the previous figures. Note the coalescence of the effects of reflected shocks into a single adverse pressure rise at $x=0.14$, located just behind the throat of this chosen geometry.

These inviscid Euler calculations are contrasted against the fully viscous Navier-Stokes solutions presented in Figure 38. Note for instance the

Velocity vectors in the combustor section
showing extent of separated region



Surface pressure distribution through
combustor region

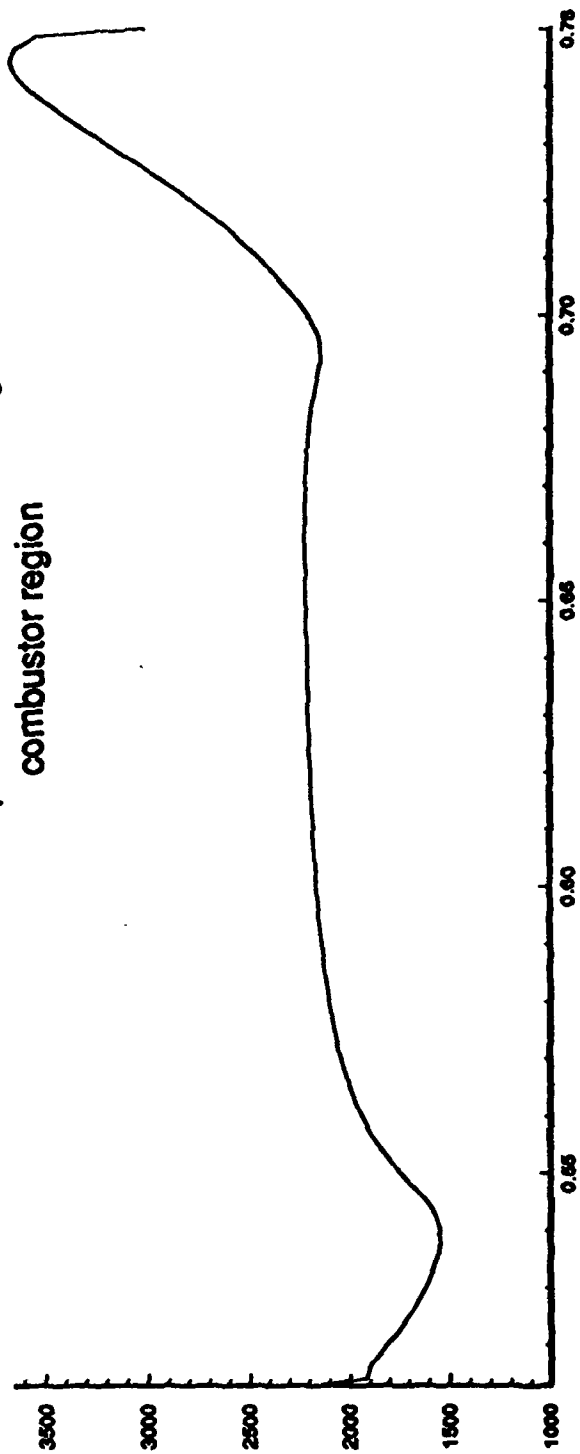


Figure 26

Time history of surface pressure
in the combustor region

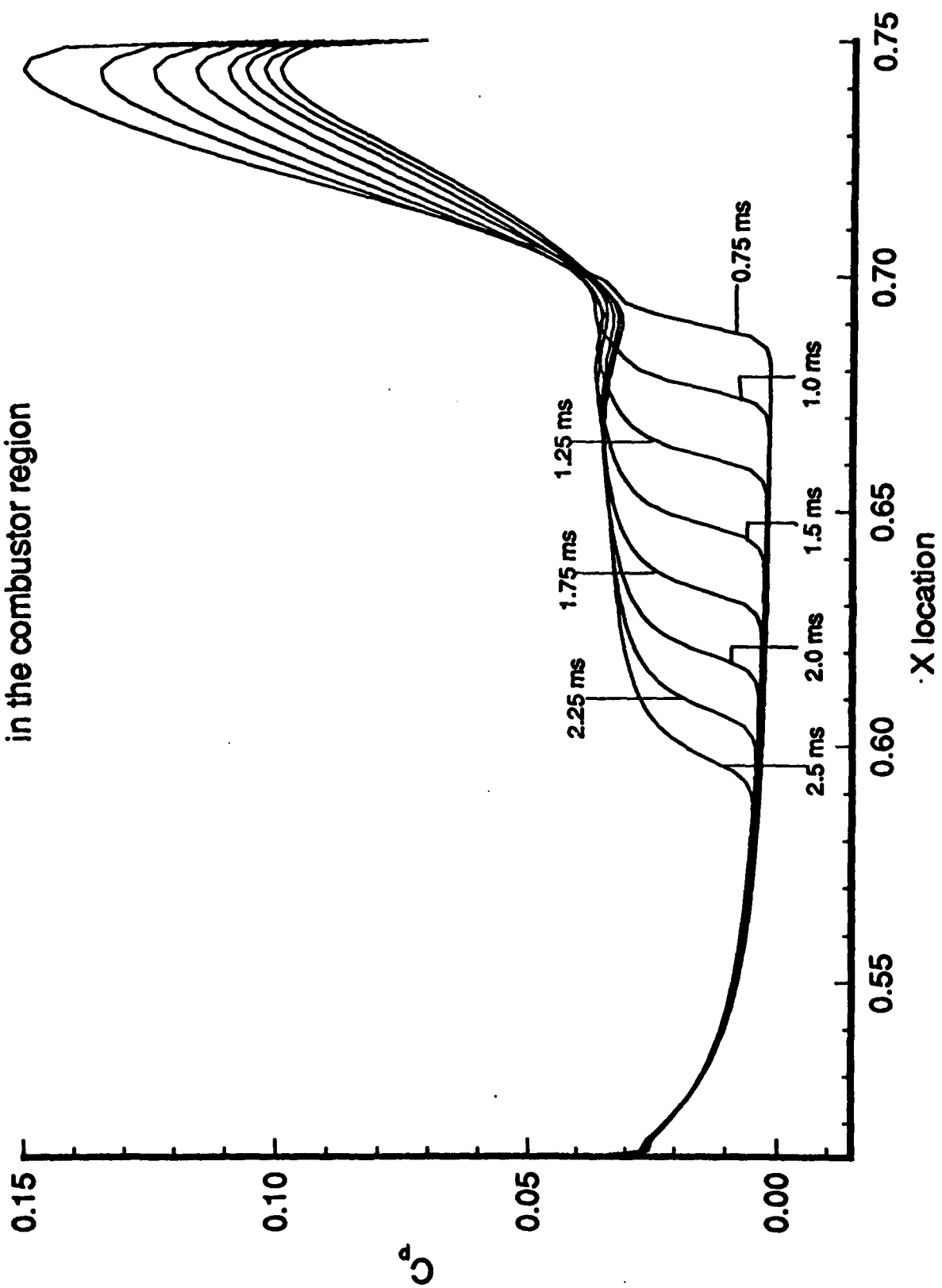


Figure 2 7

Velocity vector plot in the combustor region
at various elapsed times

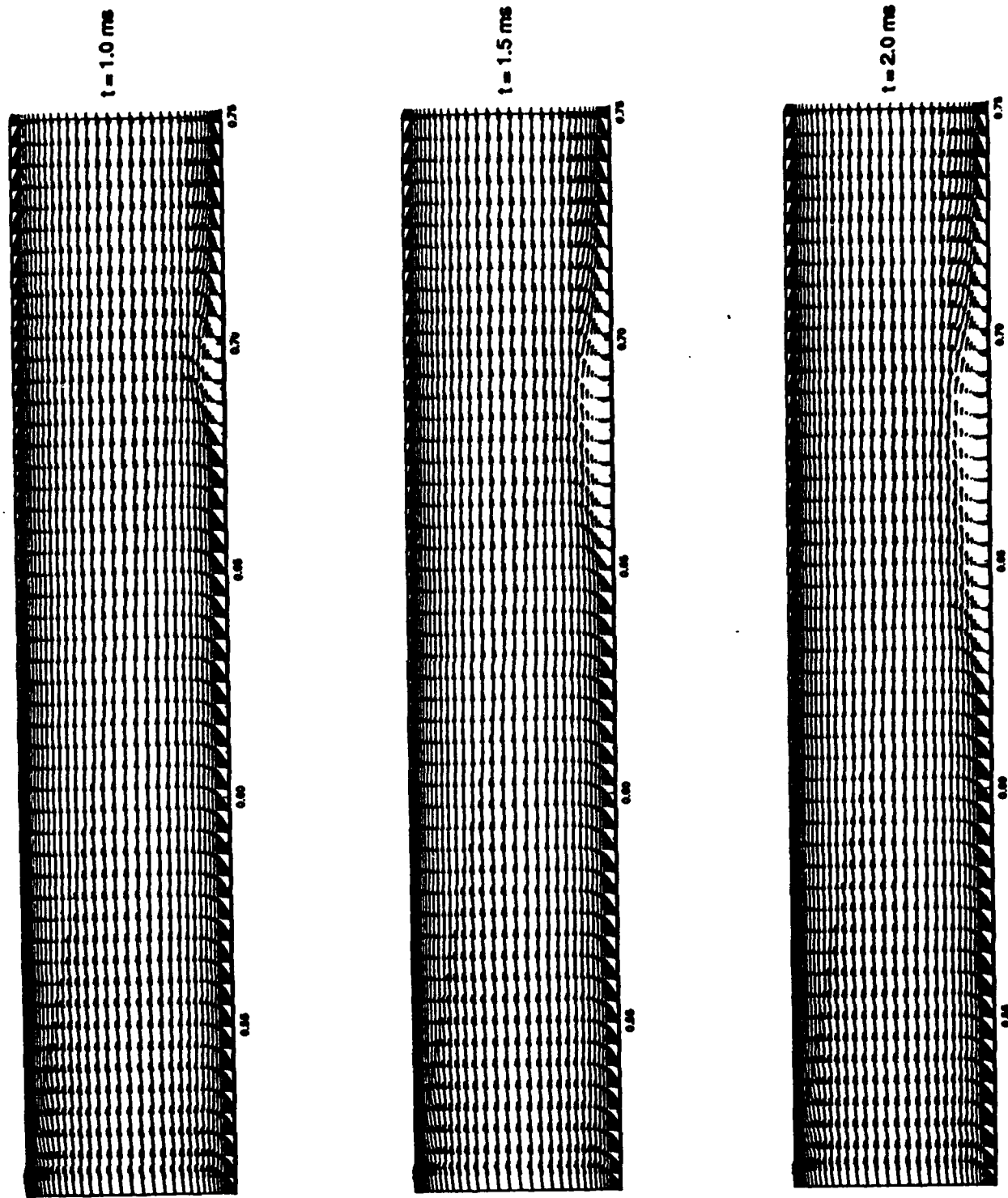


Figure 28

Density contour plot in the combustor region at various elapsed times

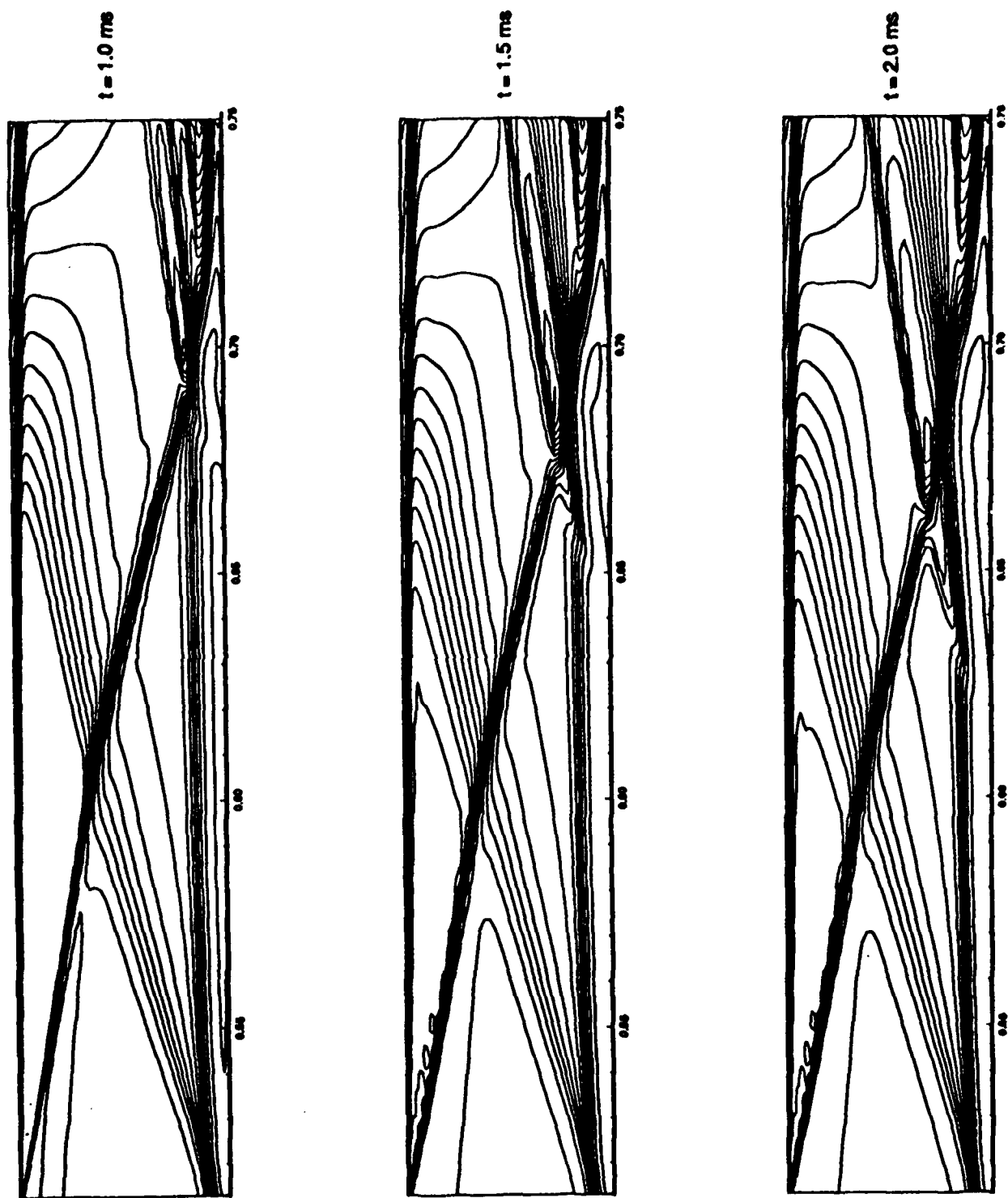


Figure 29

Grid for shock-on-lip geometry
Grid size: 151 x 51

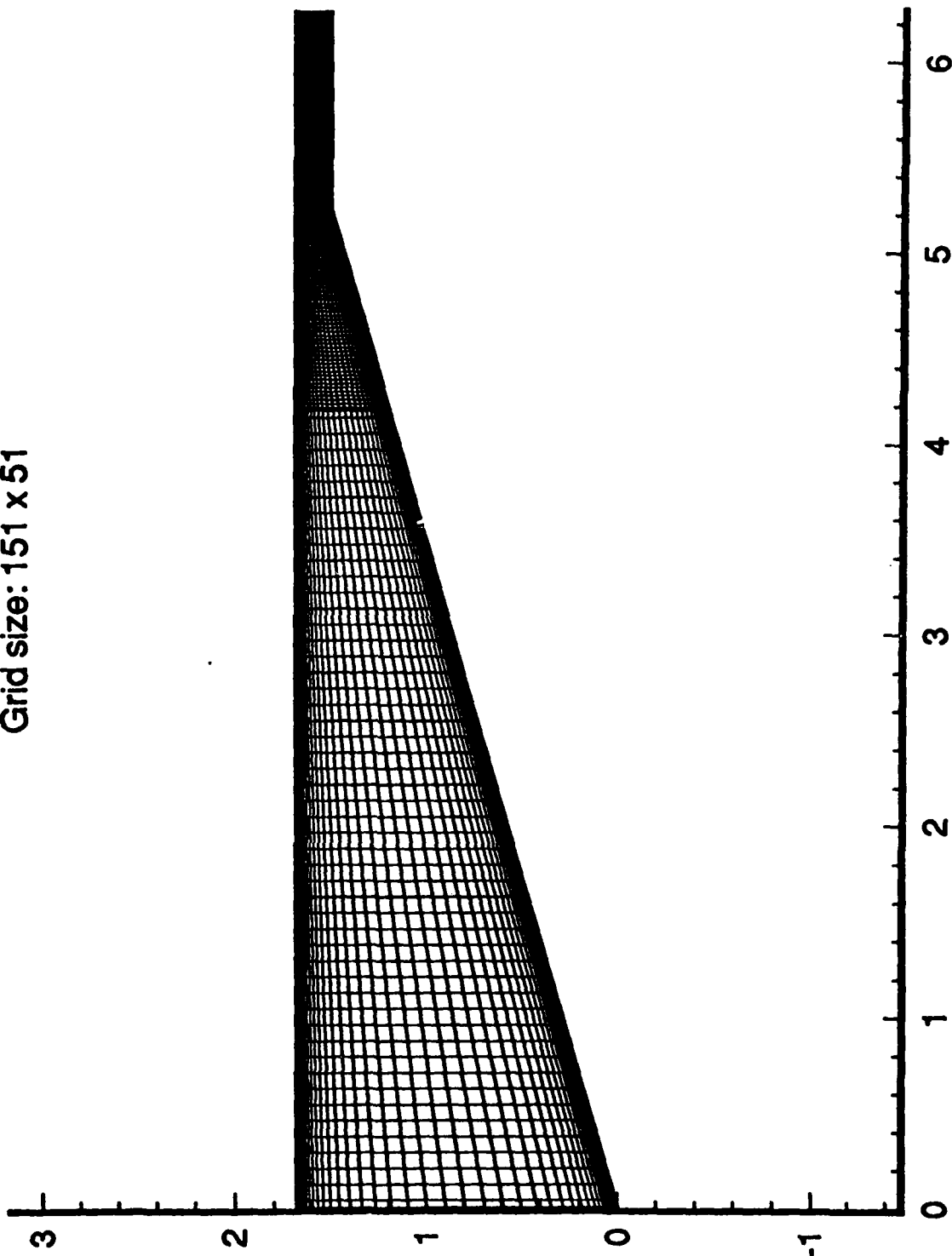


Figure 30: Computational Grid for 3-D Scramjet Engine

Leading Edge Sweepback = 30°

Grid Dimensions: 41 x 61 x 91

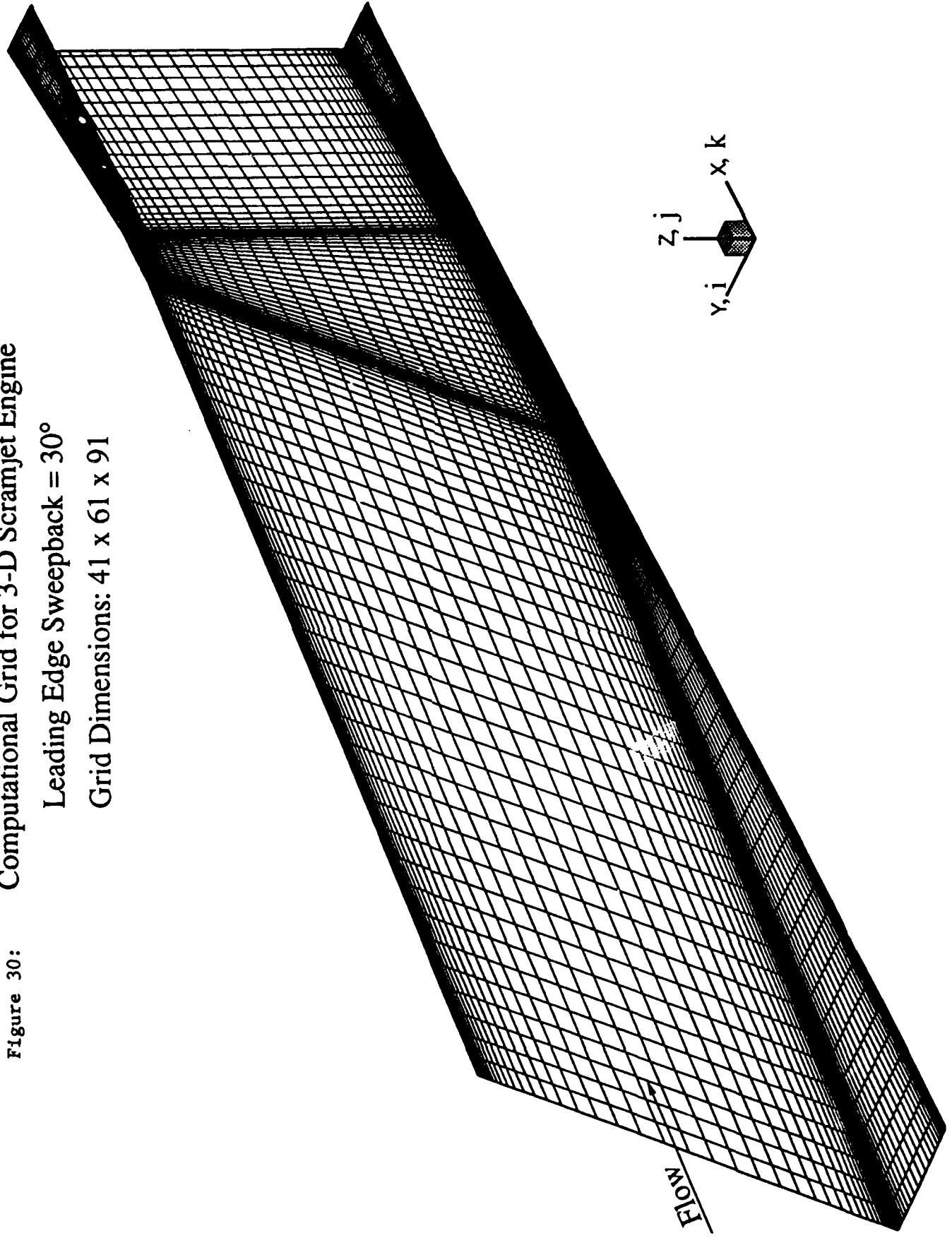


Figure 31: 3-D Scramjet Engine
Density Contours of the Euler Solution
Mach = 6.0

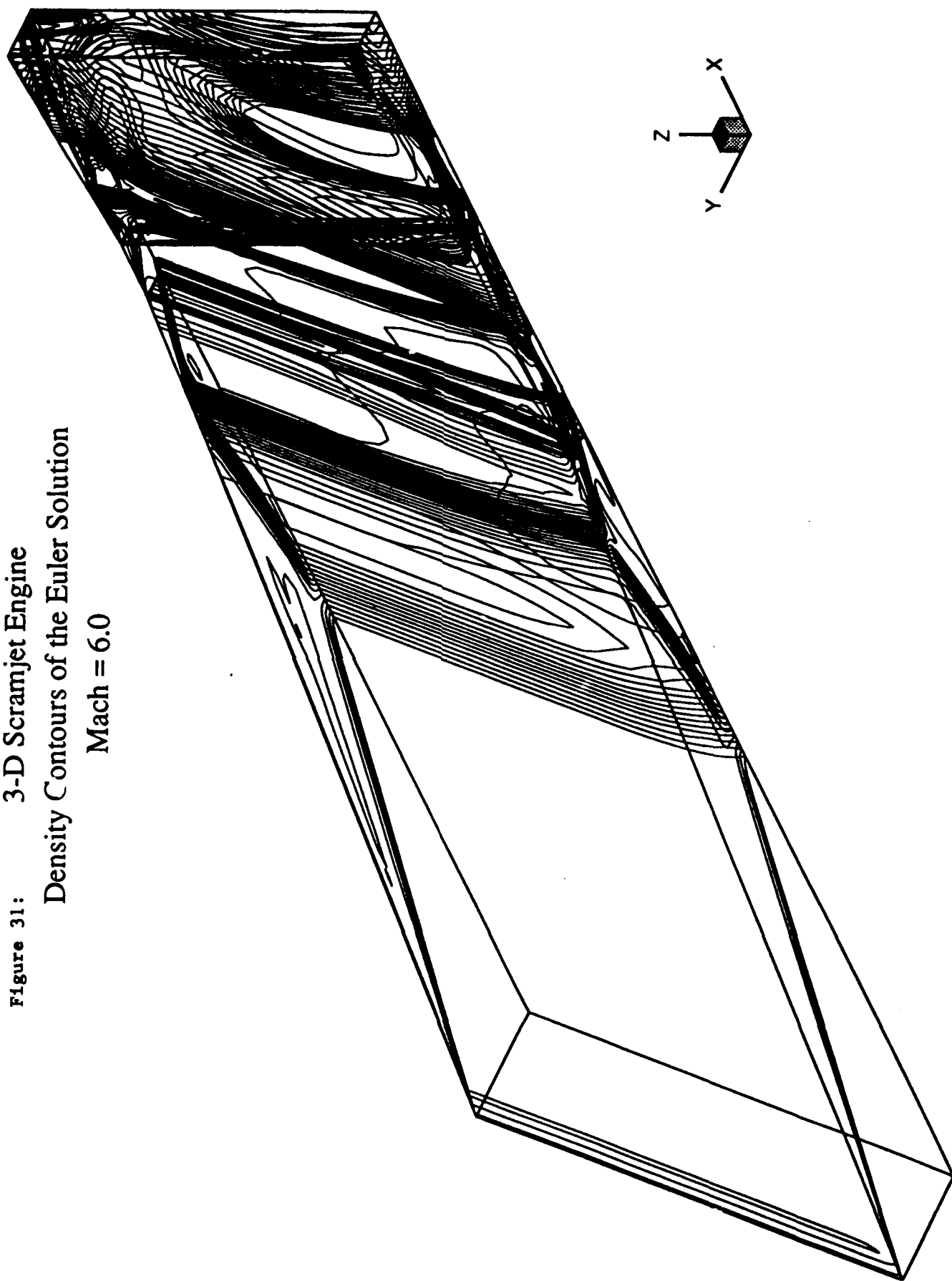


Figure 32: 3-D Scramjet Engine

Euler solution

Normalized Density Contours at $J=1$ and $J=61$

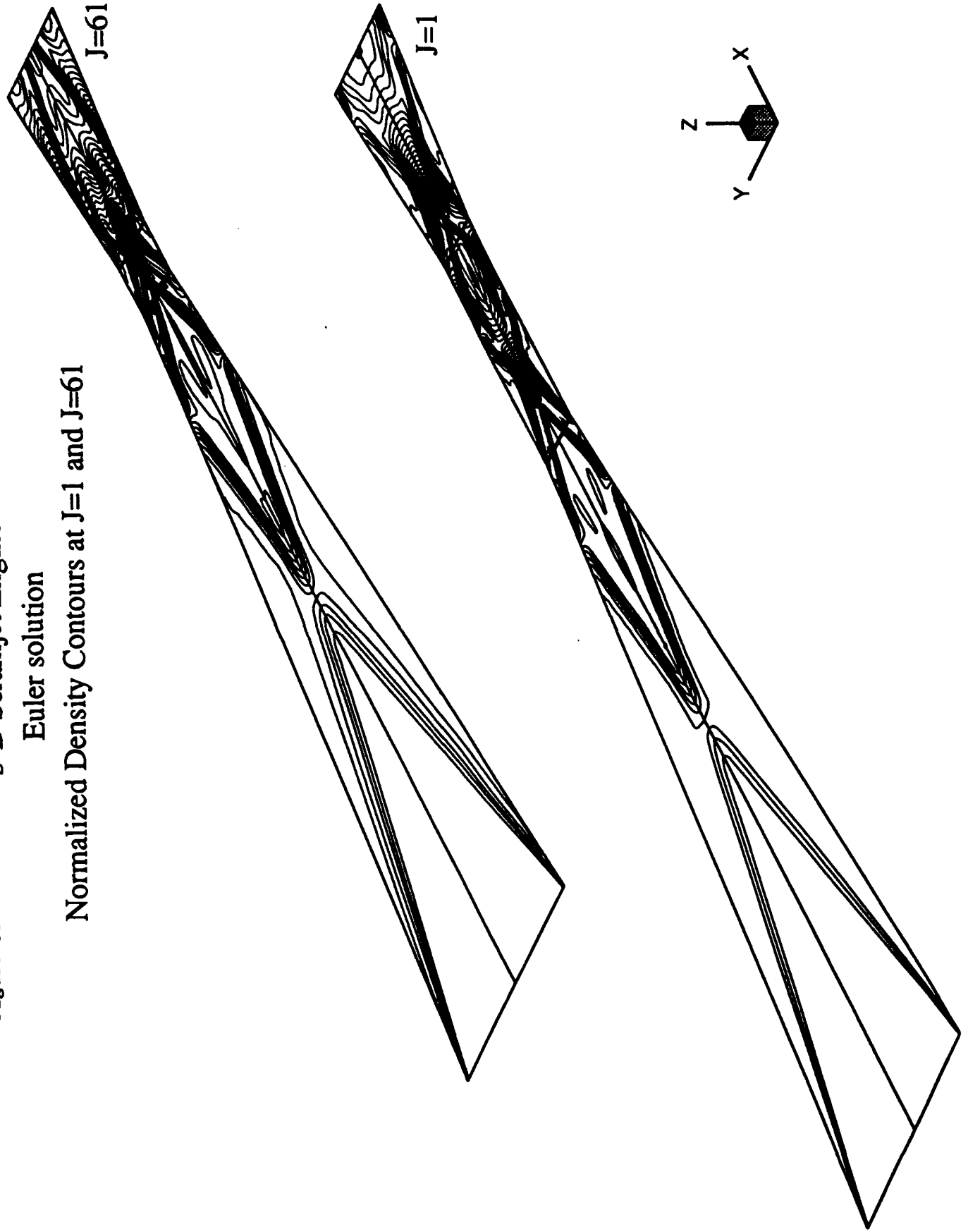


Figure 33: 3-D Scramjet Engine

Euler solution

Normalized Temperature Contours at $J=1$ and $J=61$

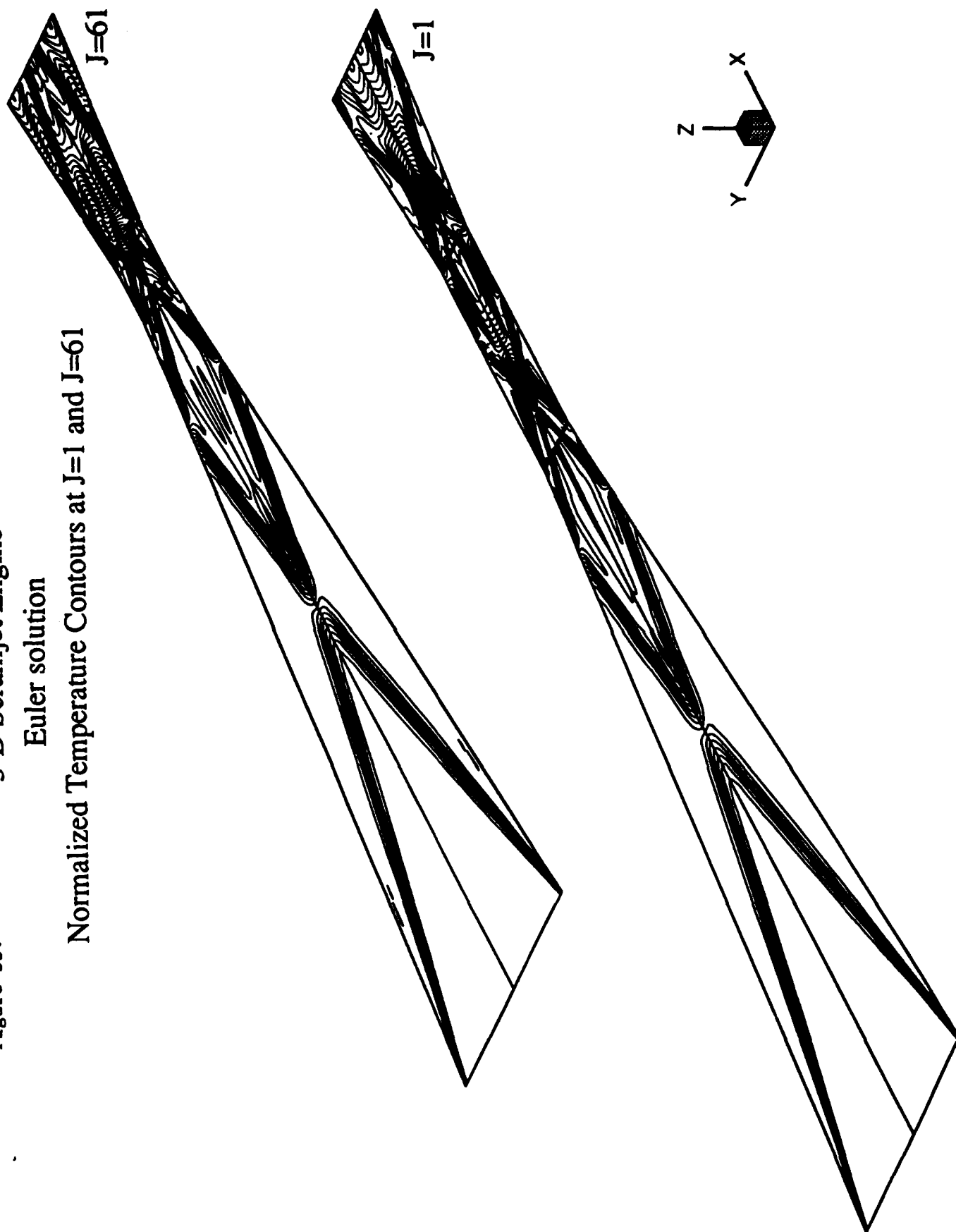


Figure 33: Euler Solution
Normalized Density Contours at $J=1$



Normalized Density Distribution through the Centerline

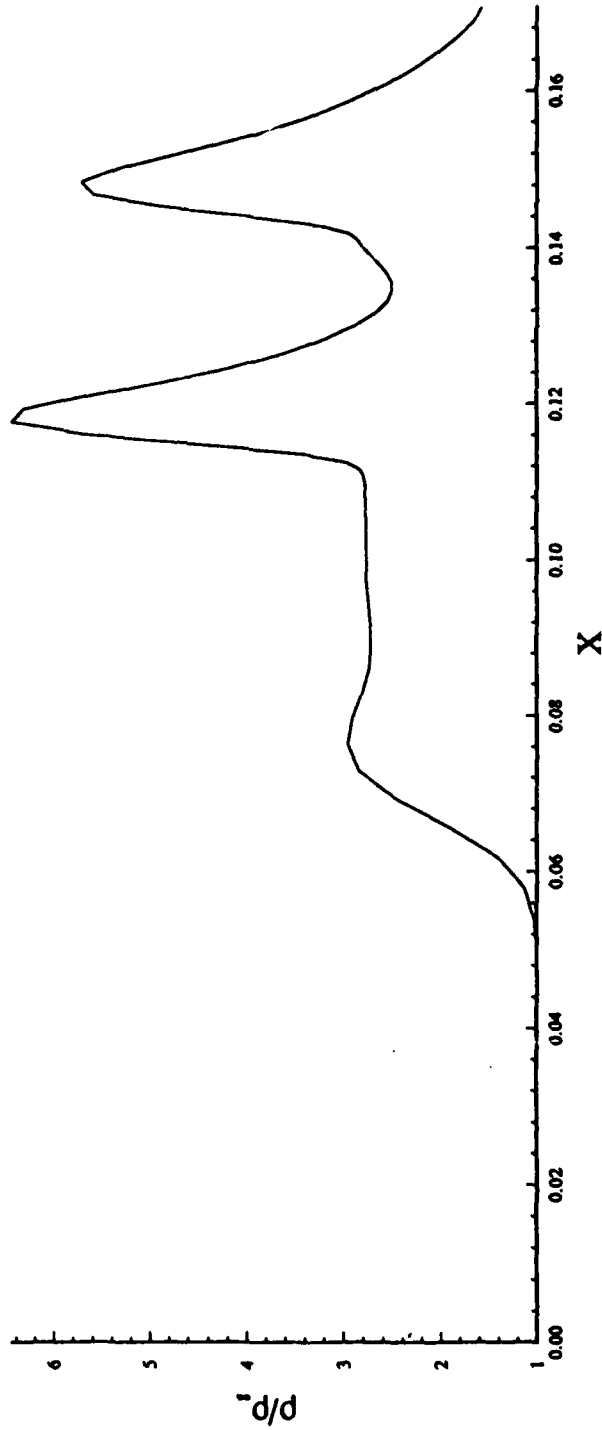


Figure 35: Euler Solution
Normalized Pressure Contours at $J=1$



Normalized Pressure Distribution through the Centerline

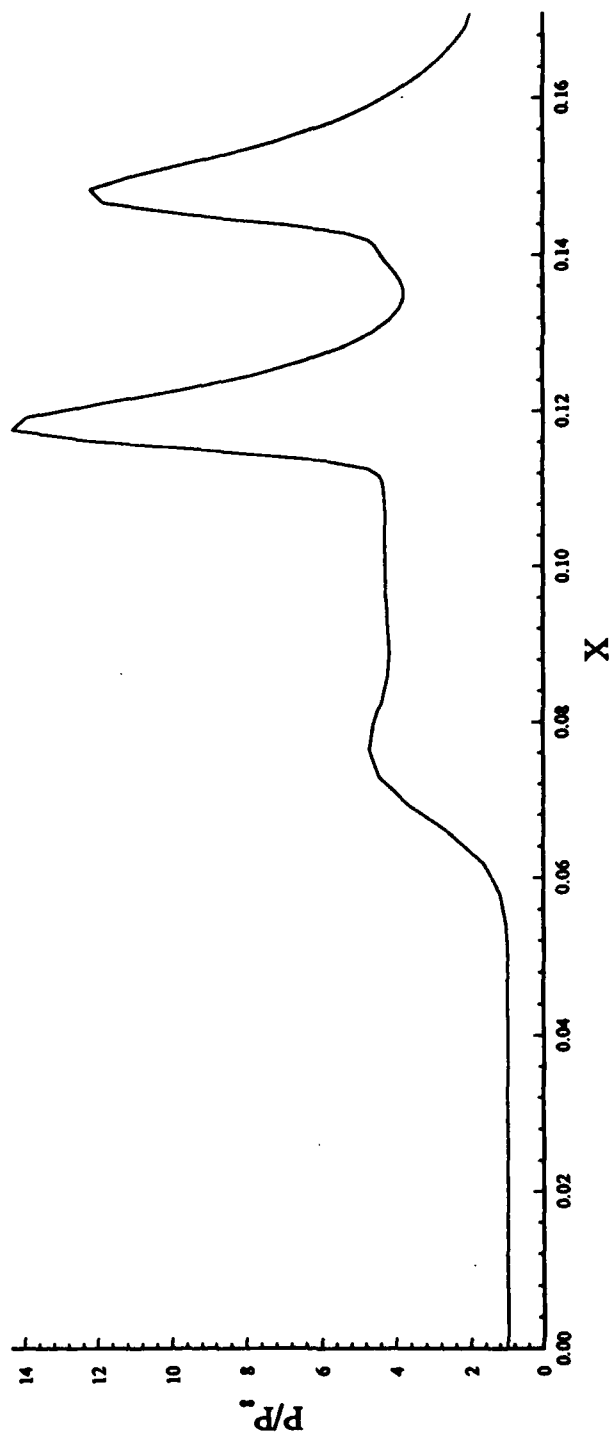


Figure 36: Euler Solution
Normalized Density Contours at $J=61$



Normalized Density Distribution through the Centerline

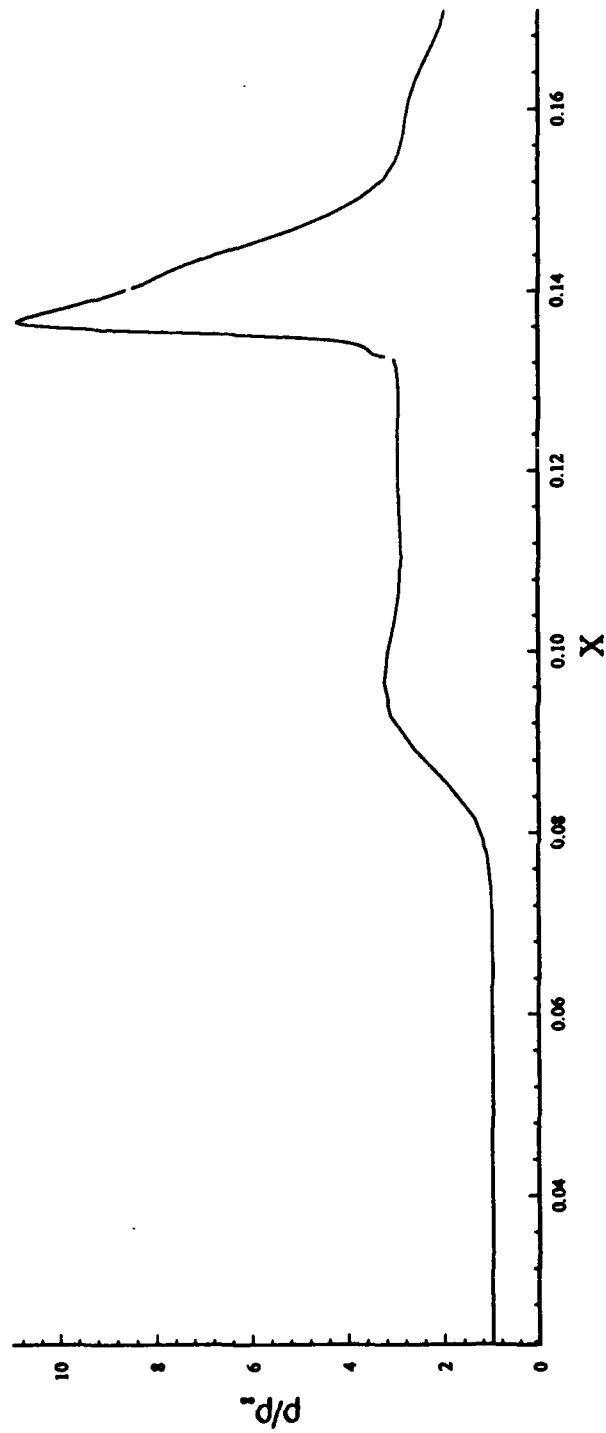


Figure 37: Euler Solution
Normalized Pressure Contours at $J=61$



Normalized Pressure Distribution through the Centerline

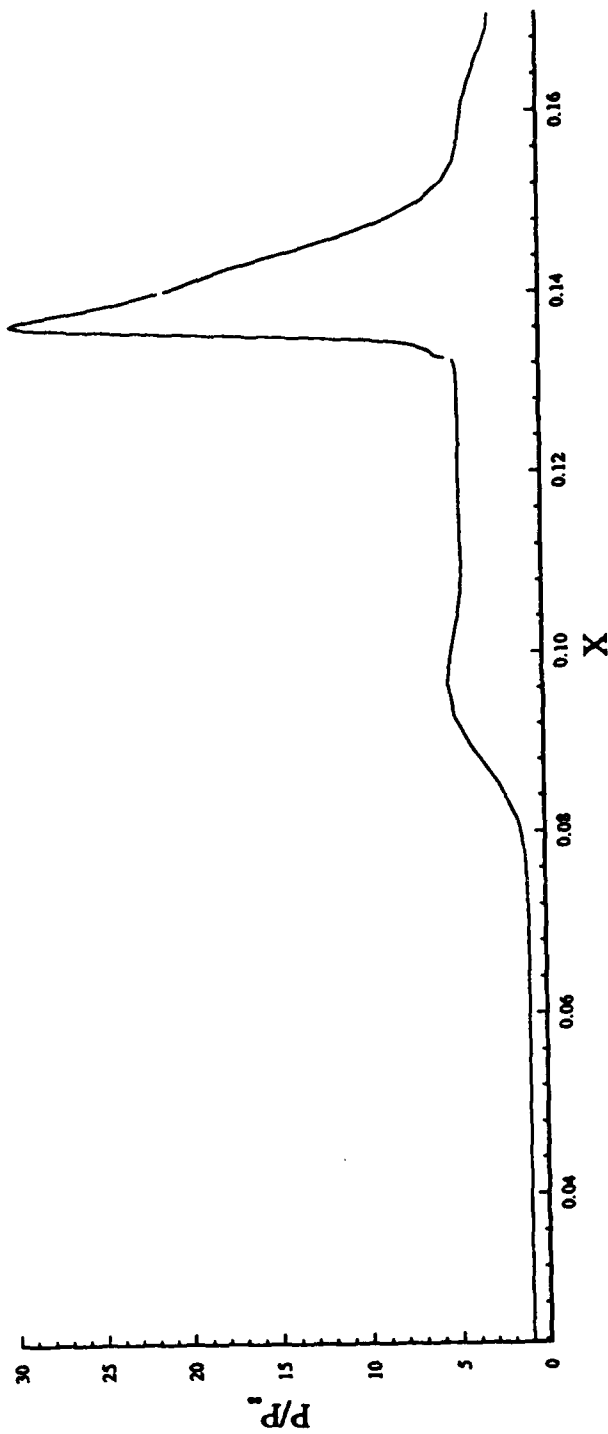


Figure 38: Navier-Stokes Solution
Density Contours at various Z locations



density contours at three z axis locations, and the noticeable differences between these solutions and the Euler results. Most important is the development of a large separation zone on the initial inlet surface, emanating from the shock-boundary layer interaction off the first reflected shockwave. This separation zone was seen to continue to grow throughout the time-accurate solution, making establishment of a steady-state result difficult. Note that this calculation was done assuming a laminar boundary layer, so the effects of boundary layer separation are undoubtedly magnified over those expected with a turbulent boundary layer.

Velocity contours presented in Figure 40 show a similar picture of separated flow with laminar flow. Note the vertical nonuniformity of the separated region, as demonstrated by the three z-axis locations plots. Velocity vectors and streamlines are shown in the following figure. Figure 42 presents density contours through the y-axis, along with temperature, x-axis velocity component, and streamlines in Figures 43-45.

A refined grid was used repeat these calculations. A $41 \times 71 \times 121$ grid, still at sweep angle of 30-degrees, was selected, as shown in Figure 46. Note that, in comparison to results shown in Figure 36 (the low-density grid), Figure 47 presents density levels of comparable shape and magnitude, though details of shock interactions are more clearly resolved on the higher-density grid. Unfortunately, fully-time accurate 3-D viscous solutions could not be run with this refined grid in a reasonable calculation time.

The next and remaining phase of this project would be the inclusion of turbulence in the calculations, to correct the highly-separated flow region and avoid the ever-expanding separation zone observed with the laminar-flow solutions. Next, with this demonstrated time-accurate calculation capability, a steady-state starting condition would be introduced downstream inside the engine.

Figure 39: Navier-Stokes Solution
Temperature Contours at various Z locations

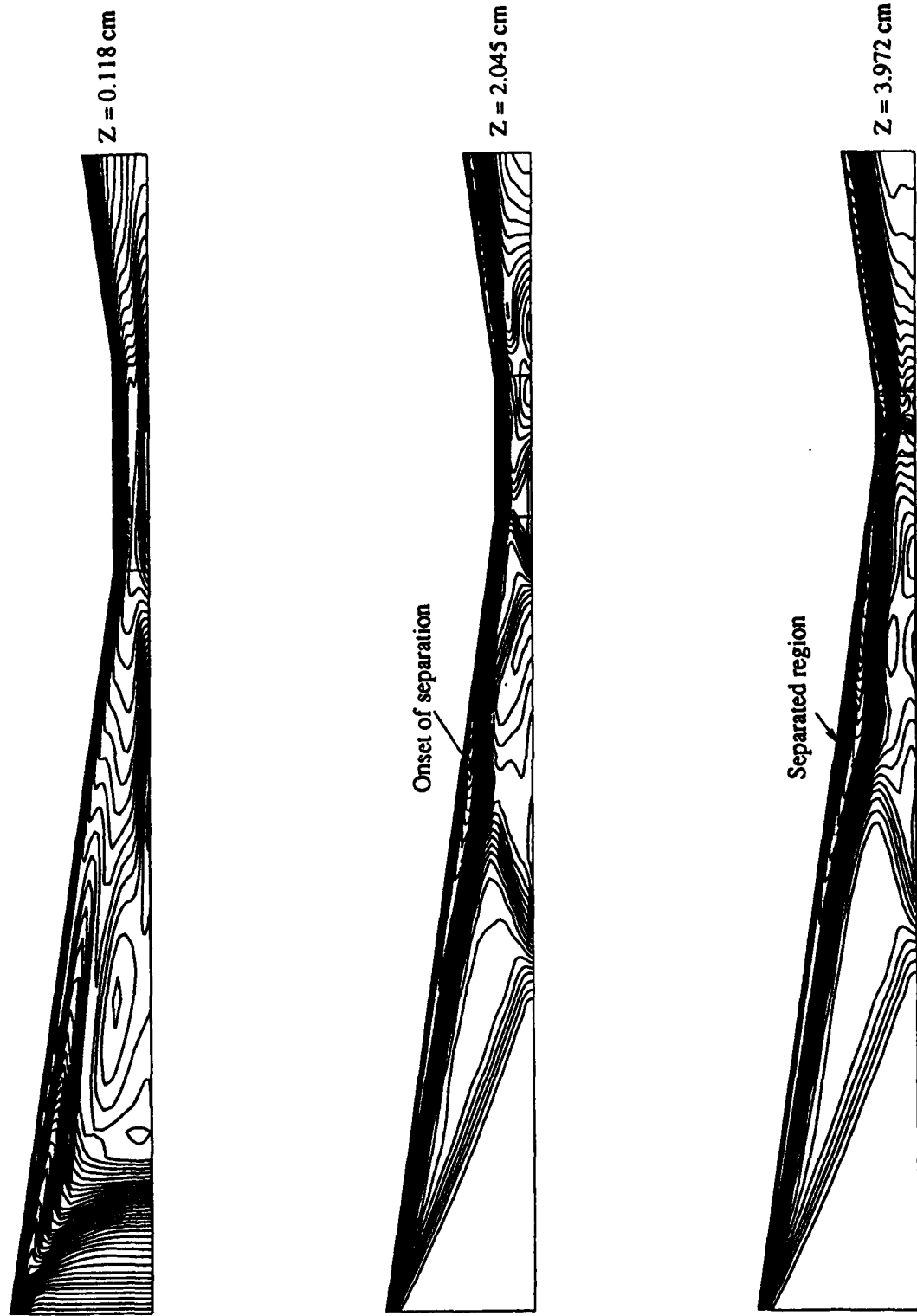


Figure 40:

Navier-Stokes Solution
U-Velocity Contours at various Z locations



Figure 41: Navier-Stokes Solution
Velocity Vectors and Streamlines at various Z locations

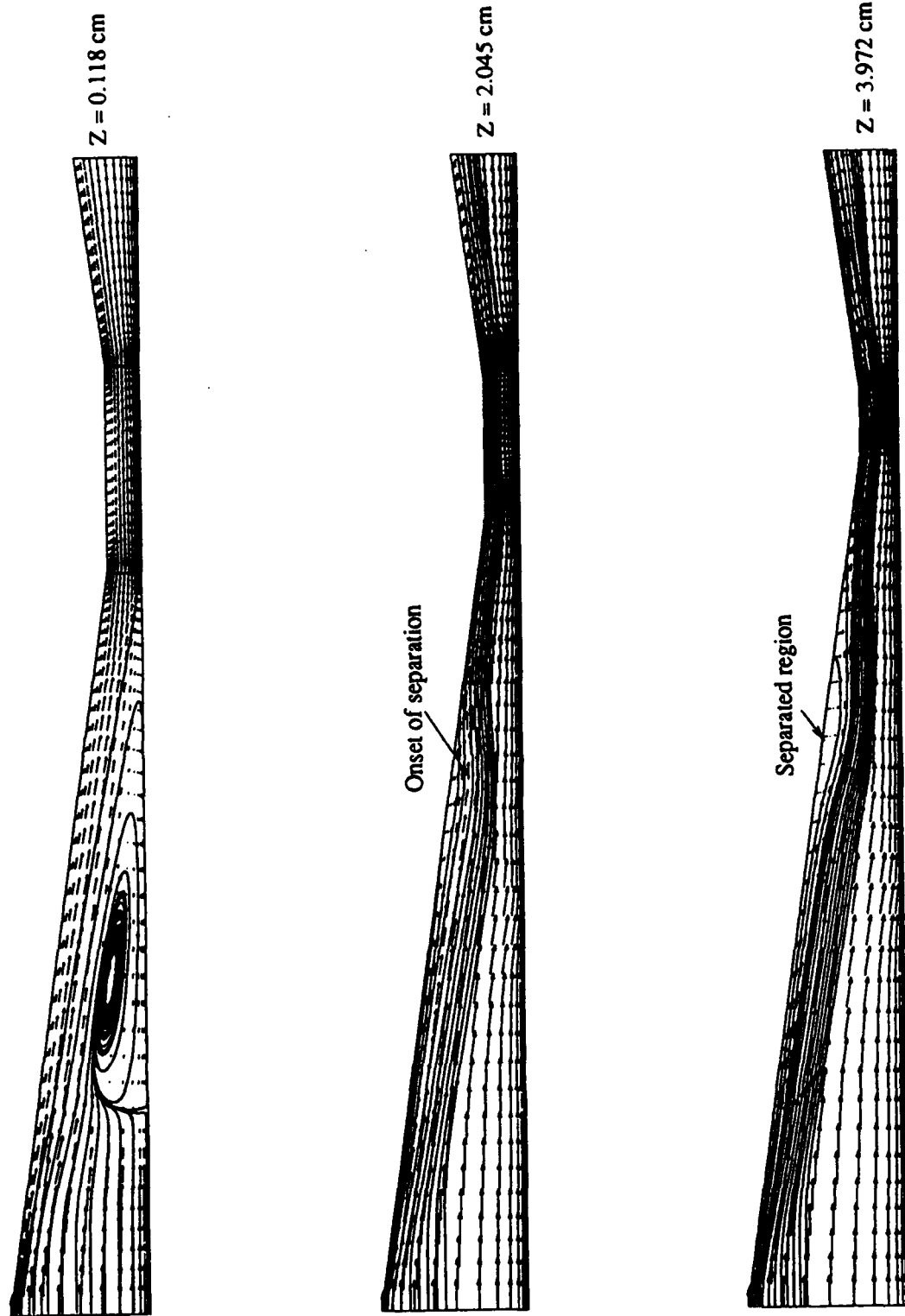
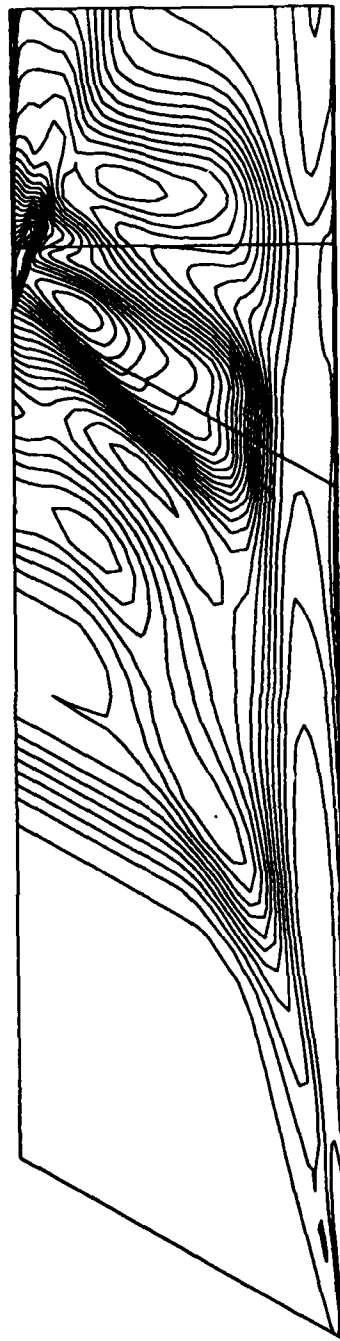
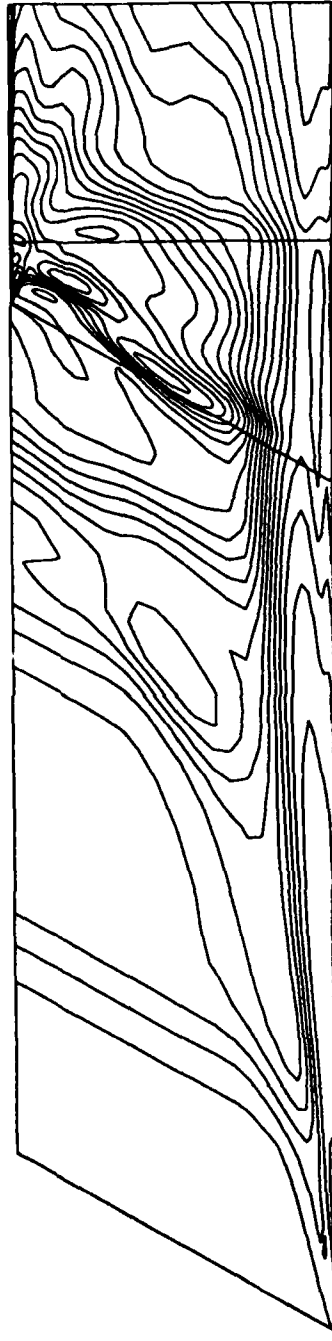


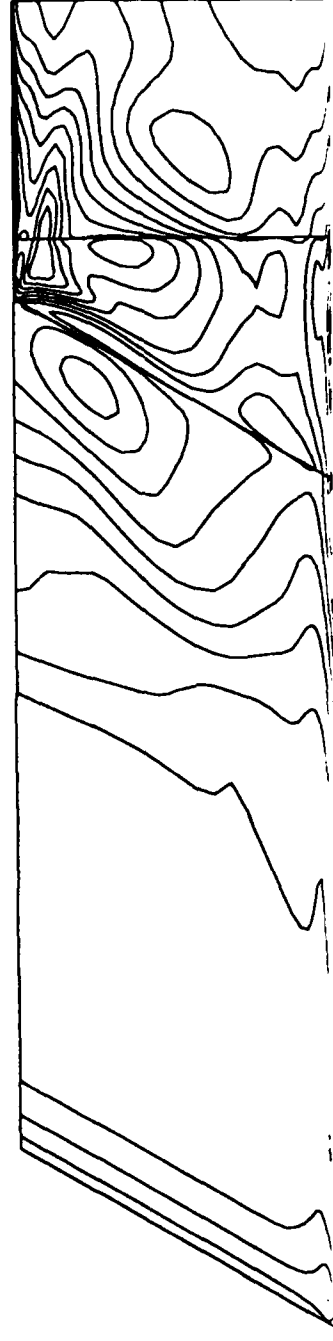
Figure 42: Navier-Stokes Solution
Density Contours at various Y locations



$Y = 0.0464 \text{ cm}$



$Y = 0.4175 \text{ cm}$



$Y = 0.8314 \text{ cm}$

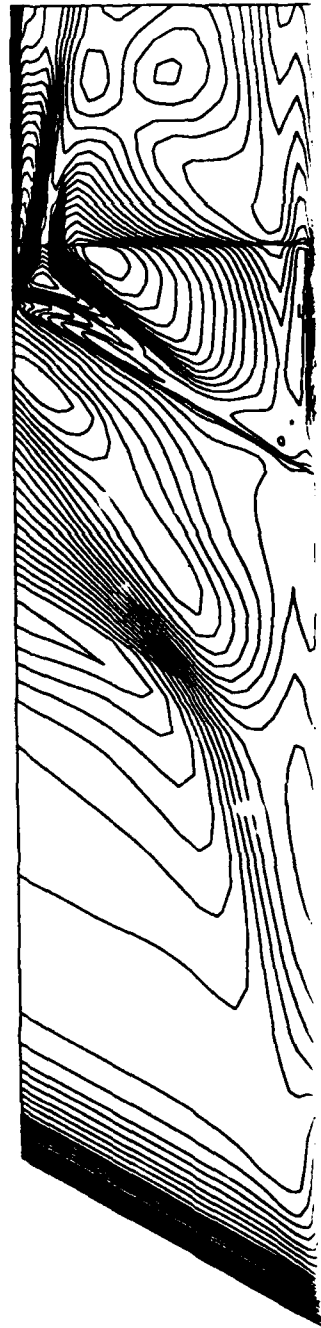
Figure 43: Navier-Stokes Solution
Temperature Contours at various Y locations



$Y = 0.0464 \text{ cm}$



$Y = 0.4175 \text{ cm}$



$Y = 0.8314 \text{ cm}$

Figure 44: Navier-Stokes Solution
U-Velocity Contours at various Y locations



$Y = 0.0464 \text{ cm}$



$Y = 0.4175 \text{ cm}$



$Y = 0.8314 \text{ cm}$

Figure 45: Navier-Stokes Solution
Velocity Vectors and Streamlines at various Y locations

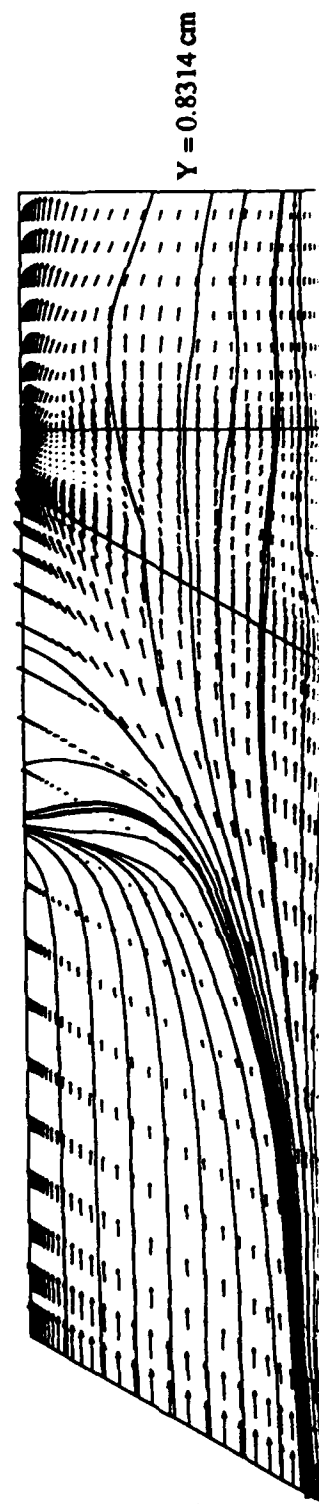
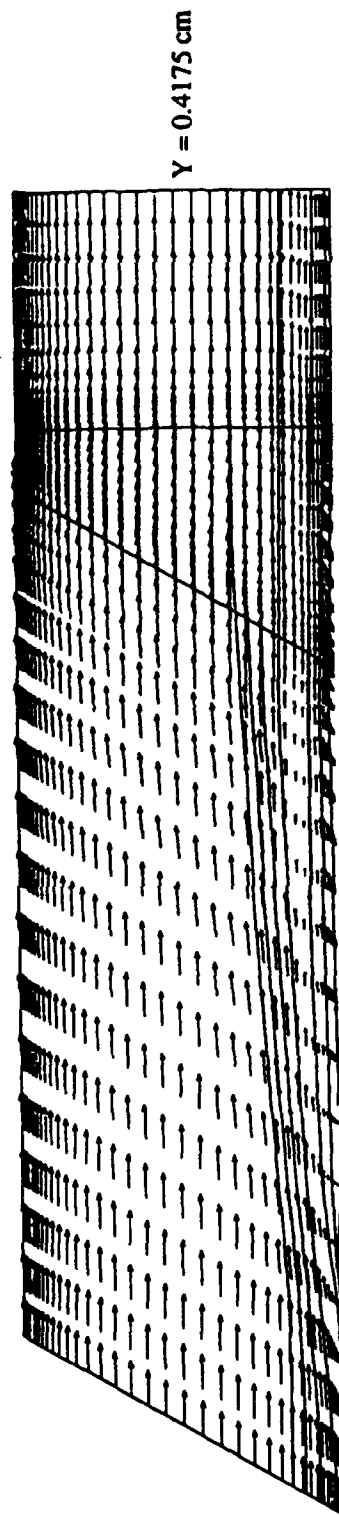
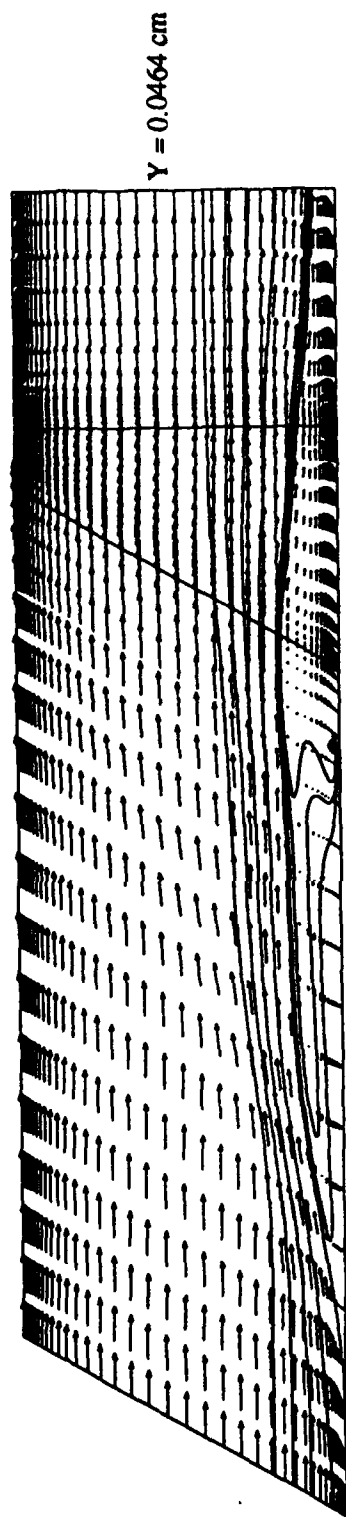


Figure 46:

Computational Grid for 3-D Scramjet Engine

Leading Edge Sweep = 30°

Grid Dimensions: 41 x 71 x 121

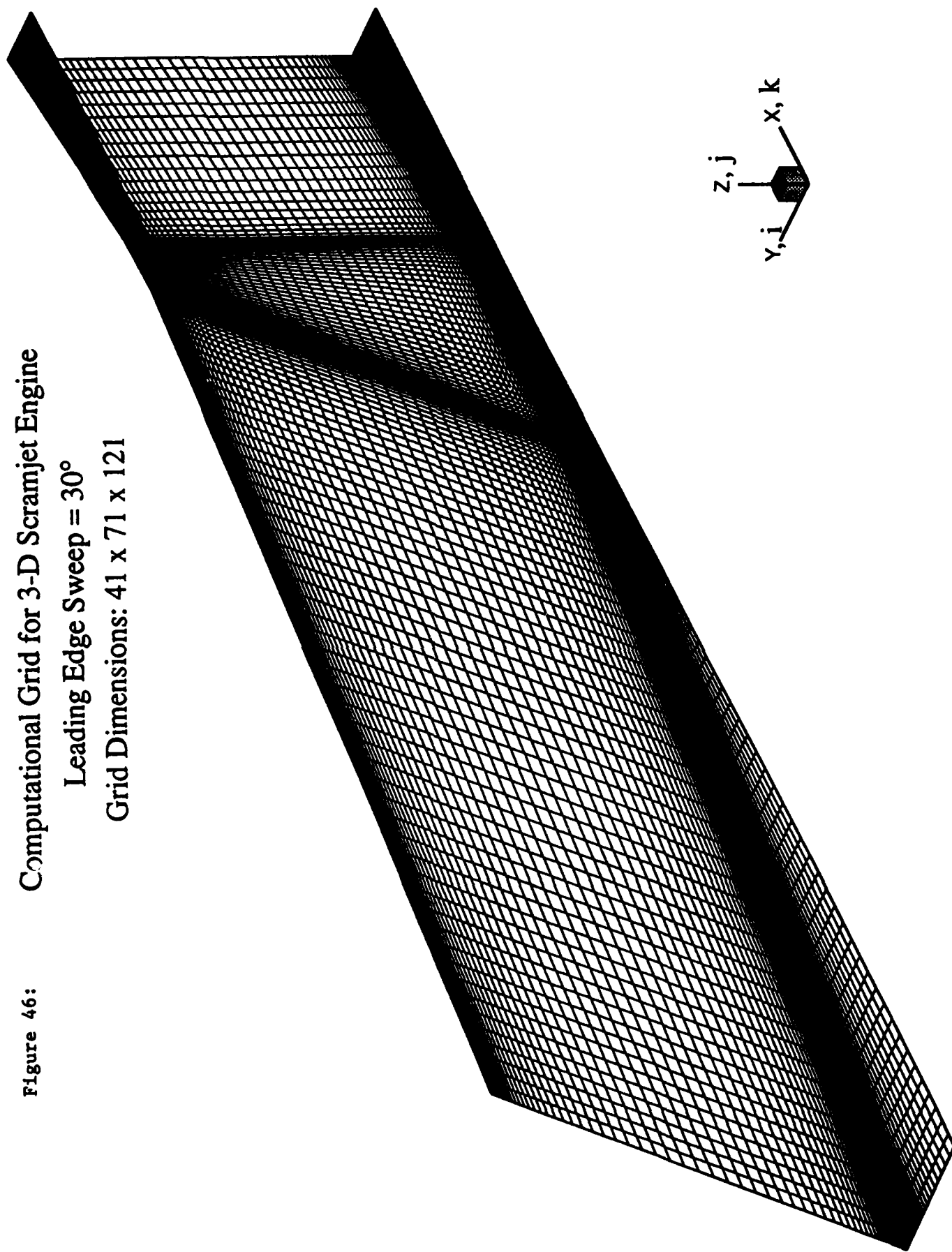


Figure 47: Euler Solution
Density Contours at various Z locations
(41 x 71 x 121)



Figure 48: Navier-Stokes Solution
Density Contours at various Z locations
(41x71x121)

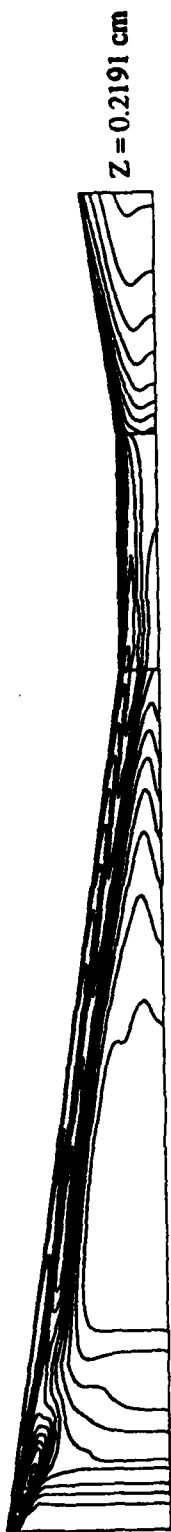


Figure 49: Navier-Stokes Solution
Temperature Contours at various Z locations
(41x71x121)



Figure 50: Navier-Stokes Solution
U-Velocity Contours at various Z locations
(41x71x121)



Figure 51: **Navier-Stokes Solution**
Velocity Vectors and Streamlines at various Z locations

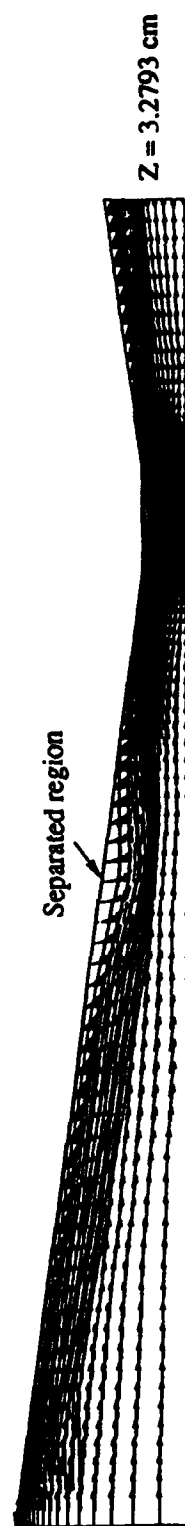
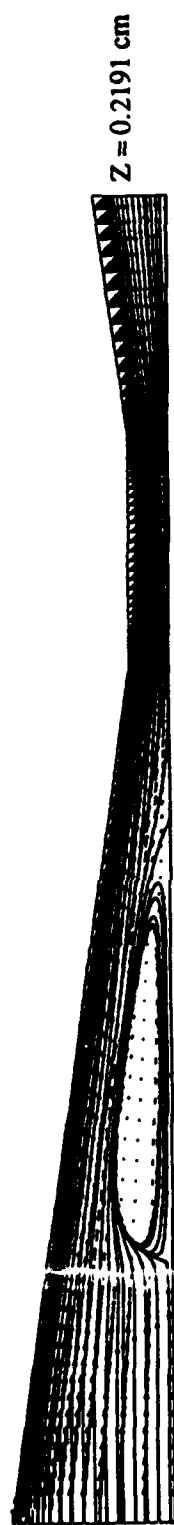


Figure 52: Navier-Stokes Solution
Density Contours at various Y locations
(41x71x121)



Figure 53: Navier-Stokes Solution
Temperature Contours at various Y locations
(41x71x121)



$I = 11$



$I = 21$



$I = 31$

Figure 54: Navier-Stokes Solution
U-Velocity Contours at various Y locations
(41x71x121)



Figure 55: Navier-Stokes Solution
Velocity Vectors and Streamlines at various Y locations
(41x71x121)

